Abstract

An analysis is presented of the H-polarization diffraction due to a material discontinuity formed by the junction of a thick dielectric half-plane with a metallic one having the same thickness. This is accomplished by first considering the solution of several subproblems. These include the direct diffraction and coupling due to a plane wave incident on a loaded open-ended parallel plate waveguide and those of radiation and reflection by a waveguide mode. The final solution for the diffraction by the metal-dielectric join is obtained by introducing a perfectly conducting stub within the loaded guide and subsequently employing the generalized scattering matrix formulation with the stub brought to the waveguide opening. All of the analysis relating to the subproblems is done via the dual integral equation approach or angular spectrum method. As expected the final expressions involve several Wiener-Hopf split functions and an efficient numerical technique for their evaluation is given in an appendix.

TABLE OF CONTENTS

I. Introduction

The problem of scattering by a join formed by a semi-infinite material slab and a thick perfectly conducting half-plane shown in Figure 1 is intimately related to those problems represented by the geometries depicted in Figure 2. These are the dielectric slab extending to infinity from a truncated parallel-plate waveguide (Figure 2a); a grounded dielectric slab with truncated upper plate (Figure 2b); and a recessed material slab in a ground plane (Figure 2c). The scope, though, of the previous work dealing with these closely allied structures has tended to focus on limited aspects relating to the investigators' specific motivations. For example, Angulo and Chang [1], Bates and Mittra [2], and Uchida and Aoki[3] have studied the configurations shown in Figures 2a and 2b with regard to surface wave excitation by the dominant parallel-plate waveguide mode. Chang and Kuester [4] considered the reflection of a TEM wave incident upon a grounded dielectric slab with truncated upper plate (Figure 2b), while Uchida and Aoki [3] and Fong [5] have investigated the radiation from the geometry in Figure 2a caused by the dominant waveguide mode. Also, with respect to the recessed material slab (Figure 2c), Kouyoumjian and Pathak [6] have examined the diffraction and reflection of the lowest order surface wave mode incident upon the junction.

To the author's knowledge, the diffracted field by the configuration involving the thick metallic dielectric junction as shown in Figure 1 has not yet been given. However, Aoki and Uchida [7] attempted a solution of the closely related problem of a dielectric-dielectric junction by introducing a Fourier series representation of the field and its derivatives at the interface of the junction. Using such an expansion, Wiener-Hopf equations were generated in terms of unknown spectral functions related to the total field. Unfortunately, the authors attempt to obtain an explicit expression for these was not realized. Instead, their computation involves an iterative solution requiring knowledge of rather complex integrals and functions whose evaluation is cumbersome and could only be done approximately.

This paper is concerned with the diffraction by the thick metallic-dielectric join illuminated with an H_z-polarized plane wave. While the scope of this invetigation appears

immediately narrowed, this is not so. As will be seen, the diffraction from the geometry in Figure 1 involves practically every aspect of the diffraction, radiation, and coupling problems associated with the geometry given in Figure 2a. Additionally, with a simple application of image theory, this knowledge translates to a characterization of the structures in Figure 2b and Figure 2c. Those aspects which are not treated herein (such as surface wave excitation) are a trivial extension of the present work and have been omitted due to the large body of previous results available. While all of this lends validity to the problem at hand as a canonical one in microstrip structures, further motivation is also derived when one considers the presence of composite materials on man-made structures where the occurrence of material-metallic junctions is common place.

The solution to the diffraction by the metallic-dielectric junction is constructed via the generalized scattering matrix formulation (GSMF) pioneered by Pace and Mittra [8]. The application of this method depends upon the solution to a number of individual problems, as shown in Figure 3. Specifically, in addition to the direct diffraction problem, one must also consider the coupling, reflection, and launching of waveguide modes at the loaded waveguide mouth. Each of these will be analyzed via the angular spectrum method (also referred to as the dual integral equation approach) [9], which provides a reduction in complexity over the parallel (but completely equivalent) Wiener-Hopf technique. A crucial step in each of these problems is the factorization of a particular complex function into components regular in the upper and lower-half complex plane. Unfortunately, the factorization cannot be done analytically and to circumvent this difficulty, an efficient numerical method is introduced which may be employed to factorize an arbitrary complex function exhibiting proper behavior.

In the first part of this paper, the formal solution to the problem is presented. After a short summary of the GSMF, the integral equations for H_z-polarization incidence are formulated in a consistent manner and boundary conditions are imposed to first extract the coupling and direct diffraction coefficients, and, subsequently, the launching and reflection coefficients. In the final part of the paper computed results are presented. The convergence

behavior of scattering patterns with respect to the included number of modes is examined, and families of computed scattering patterns are presented for selected material parameters to illustrate the scattering behavior of the dielectric-metallic join as a function of slab thickness.

II. Scattering Matrix Formulation

The problem to be considered is that of an H_z-polarized plane wave incident upon the structure shown in Figure 1 at an angle ϕ_o. In order to apply the GSMF procedure, the stub must be recessed a distance d into the waveguide, as shown in Figure 3a, forming the genesis of the individual problems illustrated in Figures 3b-3f. At the end of the procedure, the distance d is set to zero restoring the original geometry.

In accordance with the GSMF, the individual problems to be considered are as follows:

1) Evaluation of the direct diffracted field by the substructure in Figure 3b due to plane wave incidence. This field will be denoted as

$$H_{DD}(\phi, \phi_o) \sim S_{DD}(\phi, \phi_o) \frac{e^{-jk\rho}}{\sqrt{\rho}}$$

where S_{DD} is usually referred to as the diffraction coefficient and (ρ, ϕ) are the cylindrical coordinates of the far zone observation point.

2) Evaluation of the field coupled into the loaded parallel plate waveguide due to plane wave incidence as shown in Figure 3c. Hereon we will denote the field associated with the *n*th coupled mode as

$$H_{Cn}(\phi_o) = C_n(\phi_o)\, e^{-jk_n x}$$

where $C_n(\phi_o)$ is usually referred to as the coupling coefficient and k_n is the propagation constant associated with the *n*th mode.

3) Evaluation of the modal field reflected at the stub. This will be written as $\Gamma_{mn} e^{jk_m x}$ where Γ_{mn} is the stub reflection coefficient of the nth mode to the mth mode.

4) Evaluation of the reflected field at the waveguide mouth due to the *n*th mode. This will be denoted by $R_{mn} e^{-jk_m x}$ where R_{mn} is the reflection coefficient of the nth mode to the mth mode.

5) Evaluation of the far-zone radiated field due to an incident *n*th mode at the waveguide mouth. This field will be denoted as

$$H_{Ln}(\phi) \sim L_n(\phi) \frac{e^{-jk\rho}}{\sqrt{\rho}}$$

where $L_n(\phi)$ is usually referred to as the launching coefficient associated with the *n*th waveguide mode.

Accordingly, the total far zone diffracted field by the recessed stub geometry in Figure 3a is given by

$$H_z^s(\phi, \phi_o; d) \sim \left[S_{DD}(\phi, \phi_o) + S_{MOD}(\phi, \phi_o; d) \right] \frac{e^{-jk\rho}}{\sqrt{\rho}} \qquad (1)$$

where $S_{MOD}(\phi, \phi_o; d)$ is associated with the presence of the stub and, therefore, includes the contribution of the modal fields within the waveguide. It can be written in a matrix form as [10]

$$S_{MOD}(\phi, \phi_o; d) = [L_m(\phi)]^T \left\{ [I] - [P_{mn}][\Gamma_{mn}][P_{mn}][R_{mn}] \right\}^{-1} [P_{mn}][\Gamma_{mn}][P_{mn}][C_n(\phi)] \qquad (2)$$

in which the brackets signify column or square matrices depending on whether one or two subscripts appear, respectively. In addition, [I] denotes the identity matrix and $[P_{mn}]$ is the modal propagation matrix whose elements are given by

$$P_{mn} = \begin{cases} e^{-jk_m d} ; & m = n \\ 0 ; & m \neq n \end{cases} . \qquad (3)$$

Clearly, to obtain the far-zone scattered field by the dielectric-metallic join it is only required to set d = 0 in (1) and (2). In this case $[P_{mn}]$ reduces to the identity matrix and

$S_{MOD}(\phi, \phi_o)$ becomes

$$S_{MOD}(\phi, \phi_o) \equiv S_{MOD}(\phi, \phi_o; 0) = [L_m(\phi)]^T \left\{ [I] - [\Gamma_{mn}][R_{mn}] \right\}^{-1} [\Gamma_{mn}][C_n(\phi)] . \qquad (4)$$

III. Plane Wave Diffraction and Coupling

The plane wave

$$H_z^i = e^{jk(x\cos\phi_o + y\sin\phi_o)}$$

$$E_x^i = Z\sin\phi_o\, e^{jk(x\cos\phi_o + y\sin\phi_o)} \qquad (5)$$

$$E_y^i = -Z\cos\phi_o\, e^{jk(x\cos\phi_o + y\sin\phi_o)}$$

is assumed to be incident upon the structure in Figure 3b, where Z is the free space impedance, k is the free space wave number and ϕ_o is the angle of incidence measured from the positive x-axis.

If the perfectly conducting half-planes are removed, then the plane wave (5) will produce the total field

$$H_z^{pw} = \begin{cases} H_z^i + H_z^r & y>0 \\ H_z^m & -2t<y<0 \\ H_z^{tr} & y<-2t \end{cases} \tag{6}$$

where

$$H_z^r = R_H\, e^{jk(x\cos\phi_o - y\sin\phi_o)} \tag{7a}$$

$$H_z^m = e^{jkx\cos\phi_o}\left[\frac{(1+R_H)\sin[k'(y+2t)\sin\phi_o'] - T_H\sin(k'y\sin\phi_o')\,e^{-j2kt\sin\phi_o}}{\sin(2k't\sin\phi_o')}\right] \tag{7b}$$

$$H_z^{tr} = T_H\, e^{jk(x\cos\phi_o + y\sin\phi_o)}, \tag{7c}$$

$$R_H = \frac{R_{H0}(1 - P_b^2 P_a)}{1 - R_{H0}^2 P_b^2 P_a}, \qquad T_H = \frac{(1 - R_{H0}^2)P_b P_c}{1 - R_{H0}^2 P_b^2 P_a} \tag{8}$$

$$P_a = e^{j4\,ktcos\phi_o cot\phi_o'}, \quad P_b = e^{-j2\,k't/sin\phi_o'}, \quad P_c = e^{j2\,ktcos(\phi_o - \phi_o')/sin\phi_o'} \tag{9}$$

and R_{H0} is the usual plane wave reflection coefficient associated with a material half space having relative constitutive parameters ε_r and μ_r. In addition,

$$k' = k\sqrt{\varepsilon_r \mu_r} = \kappa k \tag{10}$$

where κ is the refraction index and ϕ_o' is defined according to Snell's law

$$k\cos\phi_o = k'\cos\phi_o' \ . \tag{11}$$

The presence of the metallic half-planes causes the generation of the additional field

$$H_z^s = \begin{cases} H_{z1}^s & y>0 \\ H_{z2}^s & -2t<y<0 \\ H_{z3}^s & y<-2t \end{cases} \quad . \tag{12}$$

These may be represented in terms of an angular spectrum of plane waves [9]. Specifically, a suitable spectral representation for them takes the form

$$H_{z1}^s = \int_C P_1(\cos\alpha)\, e^{-jk\rho\cos(\phi-\alpha)}\, d\alpha \quad , \tag{13a}$$

$$H_{z2}^s = -\int_C \left[Q_1(\cos\alpha)\, e^{-jk'\rho\cos(\phi+\alpha')} - Q_2(\cos\alpha)\, e^{-j2k't\sin\alpha'}\, e^{-jk'\rho\cos(\phi-\alpha')} \right] d\alpha \quad , \tag{13b}$$

$$H_{z3}^s = -\int_C P_2(\cos\alpha)\, e^{j2kt\sin\alpha}\, e^{-jk\rho\cos(\phi+\alpha)}\, d\alpha \quad , \tag{13c}$$

where C is the contour on which $\cos\alpha$ runs from $+\infty$ to $-\infty$ (see Figure 4) and $P_{1,2}(\cos\alpha)$ with $Q_{1,2}(\cos\alpha)$ are the spectra which must be determined via the application of the necessary boundary conditions. Note also that α and α' are different parameters whose relationship will be established later. The introduction of the factors $e^{j2kt\sin\alpha}$ and $e^{-j2k't\sin\alpha'}$ is totally arbitrary and could have been omitted. However, such factors are expected to appear in the final expressions for the spectra and are therefore included from the start in order to reduce the complexity of the resulting integral equations. The corresponding expressions for the x-directed component of the scattered electric fields are ($E_x = \frac{Z}{jk}\frac{\partial}{\partial y} H_z$)

$$E_{x1}^s = -Z\int_C \sin\alpha\, P_1(\cos\alpha)\, e^{-jk\rho\cos(\phi-\alpha)}\, d\alpha \quad , \tag{14a}$$

$$E^s_{x2} = -Z' \int_C \sin\alpha' \left[Q_1(\cos\alpha)\, e^{-jk'\rho\cos(\phi+\alpha')} + Q_2(\cos\alpha)\, e^{-j2kt\sin\alpha'} e^{-jk'\rho\cos(\phi-\alpha')} \right] d\alpha \quad ,$$

(14b)

$$E^s_{x3} = -Z \int_C \sin\alpha\, P_2(\cos\alpha)\, e^{j2kt\sin\alpha} e^{-jk\rho\cos(\phi+\alpha)} d\alpha \quad , \qquad (14c)$$

where $Z' = Z\sqrt{\frac{\mu_r}{\varepsilon_r}} = Z_n Z_o$.

Accordingly, the total field due to a plane wave incidence in the presence of the configuration in Figure 3b can be expressed as

$$H^{tot}_z = H^{pw}_z + H^s_z \qquad (15)$$

with H^{pw}_z and H^s_z as defined in (6) and (12), respectively. An exact expression for H^{pw}_z was given in (7). However, explicit knowledge of H^s_z requires the determination of the angular spectra $P_{1,2}(\cos\alpha)$ and $Q_{1,2}(\cos\alpha)$ appearing in expressions (13). This will be accomplished in the subsequent sections via application of the following boundary conditions:

1) The total tangential electric field is continuous over $-\infty<x<\infty$, $y = \begin{Bmatrix} 0 \\ -2t \end{Bmatrix}$, implying the boundary conditions

(B1) $E^s_{x1} = E^s_{x2}$ over $-\infty<x<\infty$, $y = 0$,

(B2) $E^s_{x2} = E^s_{x3}$ over $-\infty<x<\infty$, $y = -2t$,

since E^{pw}_x is already continuous.

2) The total magnetic field is continuous over $x<0$, $y = \begin{Bmatrix} 0 \\ -2t \end{Bmatrix}$, implying

(B3) $H^s_{z1} = H^s_{z2}$ over $x<0$, $y = 0$,

(B4) $H^s_{z2} = H^s_{z3}$ over $x<0$, $y = -2t$,

since H_z^{pw} is already continuous.

3) The tangential electric field vanishes on the perfectly conducting half-planes, implying

(B5) $E_x^i + E_x^r + E_{x1}^s = 0$ over $x>0$, $y = 0$,

(B6) $E_x^{tr} + E_{x3}^s = 0$ over $x>0$, $y = -2t$,

where $E_x^r = -Z \sin\phi_o H_z^r$ and $E_x^{tr} = Z \sin\phi_o H_z^{tr}$.

The application of boundary conditions (B1) and (B2) demand that

$$k\cos\alpha = k'\cos\alpha' \quad \text{or} \quad k'\sin\alpha' = k\sqrt{\kappa^2 - \cos^2\alpha} \tag{16}$$

and that

$$P_1(\cos\alpha) = \frac{1}{\varepsilon_r}\frac{\sqrt{\kappa^2 - \cos^2\alpha}}{\sin\alpha}\left[Q_1(\cos\alpha) + Q_2(\cos\alpha)\, e^{-j2kt\sqrt{\kappa^2 - \cos^2\alpha}}\right], \tag{17a}$$

$$P_2(\cos\alpha) = \frac{1}{\varepsilon_r}\frac{\sqrt{\kappa^2 - \cos^2\alpha}}{\sin\alpha}\left[Q_1(\cos\alpha)\, e^{-j2kt\sqrt{\kappa^2 - \lambda^2}} + Q_2(\cos\alpha)\right]. \tag{17b}$$

Thus, the number of unknown spectra has now been reduced from four to two, implying that a complete knowledge of the scattered field can be deduced from $Q_{1,2}(\cos\alpha)$. Additionally, the branch of $\sqrt{\kappa^2 - \cos^2\alpha}$ in (16) is chosen such that $\mathrm{Im}\left(\sqrt{\kappa^2 - \cos^2\alpha}\right) < 0$ for $0 \le \mathrm{Re}(\alpha) \le \pi$. This defines a mapping from the α-plane to the α'-plane as shown in Figure 5.

Enforcement of the boundary conditions (B3) - (B4) imply the integral equations

$$\int_C \left[P_1(\cos\alpha) + Q_1(\cos\alpha) - Q_2(\cos\alpha)\, e^{-j2k't\sin\alpha'}\right] e^{-jkx\cos\alpha}\, d\alpha = 0;\ x<0, \tag{18a}$$

$$\int_C \left[P_2(\cos\alpha) - Q_1(\cos\alpha)\, e^{-j2k't\sin\alpha'} + Q_2(\cos\alpha)\right] e^{-jkx\cos\alpha}\, d\alpha = 0;\ x<0. \tag{18b}$$

When (17) is incorporated into (18) with a change of variable from α to $\lambda = \cos\alpha$, and the resulting equations are added and subtracted, we obtain the decoupled set

$$\int_{-\infty}^{\infty} \left[Q_1(\lambda) + Q_2(\lambda) \right] \frac{\sqrt{\kappa^2 - \lambda^2}}{1 - \lambda^2} F_3(\lambda)\, e^{-jkx\lambda}\, d\lambda = 0; \; x<0 \quad , \tag{19a}$$

$$\int_{-\infty}^{\infty} \left[Q_1(\lambda) - Q_2(\lambda) \right] \frac{\sqrt{\kappa^2 - \lambda^2}}{1 - \lambda^2} F_4(\lambda)\, e^{-jkx\lambda}\, d\lambda = 0; \; x<0 \quad , \tag{19b}$$

where

$$F_3(\lambda) = \frac{2\left[\sqrt{\lambda^2 - \kappa^2}\, \cosh\left(kt\sqrt{\lambda^2 - \kappa^2}\right) + \varepsilon_r \sqrt{\lambda^2 - 1}\, \sinh\left(kt\sqrt{\lambda^2 - \kappa^2}\right) \right]}{(\varepsilon_r + 1)\sqrt{\lambda^2 - \kappa^2}\; e^{kt\sqrt{\lambda^2 - \kappa^2}}} \tag{20a}$$

and

$$F_4(\lambda) = \frac{2\left[\sqrt{\lambda^2 - \kappa^2}\, \sinh\left(kt\sqrt{\lambda^2 - \kappa^2}\right) + \varepsilon_r \sqrt{\lambda^2 - 1}\, \cosh\left(kt\sqrt{\lambda^2 - \kappa^2}\right) \right]}{(\varepsilon_r + 1)\sqrt{\lambda^2 - \kappa^2}\; e^{kt\sqrt{\lambda^2 - \kappa^2}}} \; . \tag{20b}$$

Note that in deriving (20), we have defined $\sqrt{\lambda^2 - 1} = j\sqrt{1 - \lambda^2}$ and $\sqrt{\lambda^2 - \kappa^2} = j\sqrt{\kappa^2 - \lambda^2}$. In addition, the complex λ-plane defined by the mapping $\lambda = \cos\alpha$ is shown in Figure 6.

The boundary conditions (B5) and (B6) imply the integral equations

$$\int_{-\infty}^{\infty} P_1(\lambda)\, e^{-jkx\lambda}\, d\lambda = \sin\phi_o\, (1 - R_H)\, e^{jkx\cos\phi_o} \qquad ; x > 0 \quad , \tag{21a}$$

$$\int_{-\infty}^{\infty} P_2(\lambda)\, e^{-jkx\lambda}\, d\lambda = \sin\phi_o\, T_H\, e^{-j2kt\sin\phi_o}\, e^{jkx\cos\phi_o} \qquad ; x > 0 \quad . \tag{21b}$$

Substituting (17) into (21) and adding and subtracting the resulting equations we find

$$\int_{-\infty}^{\infty} [\, Q_1(\lambda) + Q_2(\lambda) \,] \frac{\sqrt{\kappa^2 - \lambda^2}}{\sqrt{1-\lambda^2}} F_1(\lambda)\, e^{-jkx\lambda}\, d\lambda = \varepsilon_r \sin\phi_o \left(1 - R_H + T_H e^{-j2kt\, \sin\phi_o}\right) e^{jkx\, \cos\phi_o} \quad ; x > 0 \ ,$$

(22a)

$$\int_{-\infty}^{\infty} [\, Q_1(\lambda) - Q_2(\lambda) \,] \frac{\sqrt{\kappa^2 - \lambda^2}}{\sqrt{1-\lambda^2}} F_2(\lambda)\, e^{-jkx\lambda}\, d\lambda = \varepsilon_r \sin\phi_o \left(1 - R_H - T_H e^{-j2kt\, \sin\phi_o}\right) e^{jkx\, \cos\phi_o} \quad ; x > 0 \ ,$$

(22b)

with

$$F_{\substack{1\\2}}(\lambda) = 1 \pm e^{-j2kt\sqrt{\kappa^2 - \lambda^2}} \ . \tag{23}$$

The dual integral equations (19) and (22) are now sufficient for a solution of $Q_1(\lambda) \pm Q_2(\lambda)$. However, before such a solution can be pursued, it is necessary that $F_{1,2}(\lambda)$ and $F_{3,4}(\lambda)$ be factorized into functions regular (i.e. free of poles, zeros and branch points) in the upper and lower half of the complex λ-plane. Utilizing the factorization procedure outlined in Noble [11], $F_{1,2}(\lambda)$ may be factorized as

$$F_{\substack{1\\2}}(\lambda) = L_{\substack{1\\2}}(\lambda)\, U_{\substack{1\\2}}(\lambda) \ , \tag{24}$$

where the functions denoted by L/U are regular in the upper/lower half of the λ–plane. Expressions for $L_{1,2}(\lambda)$, $U_{1,2}(\lambda)$ are given in Appendix A. On the other hand, the factorization of $F_{3,4}(\lambda)$ into

$$F_{\substack{3\\4}}(\lambda) = L_{\substack{3\\4}}(\lambda)\, U_{\substack{3\\4}}(\lambda) \tag{25}$$

is much more involved. Notwithstanding, numerical and analytical techniques do exist for accomplishing it [2,13]. The factorization of $F_{3,4}(\lambda)$ herein will be accomplished through a recently developed numerical procedure with the final expressions of $U_{3,4}(\lambda)$ and $L_{3,4}(\lambda)$ in terms of an integral over the convenient finite interval [0,1], as given in Appendix B. The utility of this numerical technique also stems from the fact that it may be applied to a very wide class of complex functions with no special preconditioning of these necessary (i.e. involved treatment of poles, etc.). In passing, we note that for the special case of $\kappa = 1$, $F_{1,2}(\lambda)$ reduce to functions already encountered [12] and $F_{3,4}(\lambda) = 1$.

Using the factorizations (24) and (25) we many now proceed for a solution of the spectra $Q_{1,2}(\lambda)$. Since (19) holds for $x < 0$, we may close the path of integration by a semi-infinite contour in the upper half of the λ-plane and employ Cauchy's theorem along with (25) to deduce that

$$[Q_1(\lambda) \pm Q_2(\lambda)] \frac{\sqrt{\kappa^2 - \lambda^2}}{1-\lambda^2} L_{\substack{3 \\ 4}}(\lambda) U_{\substack{3 \\ 4}}(\lambda) = U_{\substack{A \\ B}}(\lambda) \tag{26}$$

where $U_{A,B}(\lambda)$ are unknown functions regular in the upper half of the λ-plane. Similarly, (22) holds for $x > 0$ enabling us to close the path of integration by a semi-infinite contour in the lower half of the λ-plane and again invoke Cauchy's theorem along with (24) to obtain

$$[Q_1(\lambda) \pm Q_2(\lambda)] \frac{\sqrt{\kappa^2 - \lambda^2}}{\sqrt{1-\lambda^2}} L_{\substack{1 \\ 2}}(\lambda) U_{\substack{1 \\ 2}}(\lambda) = \frac{\varepsilon_r}{-2\pi j} \frac{(1 - R_H \pm T_H e^{-j2kt \sin\phi_o}) \sin\phi_o}{\lambda + \cos\phi_o}$$

$$\frac{L_{\substack{A\\B}}(\lambda)}{L_{\substack{A\\B}}(-\cos\phi_o)} \tag{27}$$

where $L_{A,B}(\lambda)$ are unknown functions regular in the lower half λ-plane. Substituting (26) into (27) it may be deduced that

$$L_{\substack{A\\B}}(\lambda) = \frac{\sqrt{1+\lambda}\; L_{\substack{1\\2}}(\lambda)}{L_{\substack{3\\4}}(\lambda)}\ , \tag{28}$$

$$U_{\substack{A\\B}}(\lambda) = \frac{j\varepsilon_r}{2\pi}(1 - R_H \pm T_H e^{-j2kt\,\sin\phi_o}) \frac{\sqrt{2}\cos(\phi_o/2)}{\sqrt{1-\lambda}} \frac{1}{\lambda+\lambda_o} \frac{U_{\substack{3\\4}}(\lambda_o)\, U_{\substack{3\\4}}(\lambda)}{U_{\substack{1\\2}}(\lambda_o)\, U_{\substack{1\\2}}(\lambda)}\ , \tag{29}$$

since $L_{A,B}$ and $U_{A,B}$ are associated with different regions of regularity. Finally from (29) and (26) it follows that

$$Q_{\substack{1\\2}}(\lambda) = \frac{-\varepsilon_r}{4\pi j} \frac{\sqrt{1-\lambda^2}}{\sqrt{\kappa^2-\lambda^2}} \frac{\sqrt{2}\cos(\phi_o/2)\sqrt{1+\lambda}}{\lambda+\lambda_o} \left\{ (1 - R_H + T_H e^{-j2kt\,\sin\phi_o}) \frac{U_3(\lambda_o)}{L_3(\lambda)\, U_1(\lambda)\, U_1(\lambda_o)} \right.$$

$$\left. \pm (1 - R_H - T_H e^{-j2kt\,\sin\phi_o}) \frac{U_4(\lambda_o)}{L_4(\lambda)\, U_2(\lambda)\, U_2(\lambda_o)} \right\}\ , \tag{30}$$

and from (17)

$$P_{\substack{1\\2}}(\lambda) = \frac{-1}{4\pi j} \frac{\sqrt{2}\cos(\phi_o/2)\sqrt{1+\lambda}}{\lambda+\lambda_o} \left\{ (1 - R_H + T_H e^{-j2kt\,\sin\phi_o}) \frac{L_1(\lambda)\, U_3(\lambda_o)}{L_3(\lambda)\, U_1(\lambda_o)} \right.$$

$$\left. \pm (1 - R_H - T_H e^{-j2kt\,\sin\phi_o}) \frac{L_2(\lambda)\, U_4(\lambda_o)}{L_4(\lambda)\, U_2(\lambda_o)} \right\}\ . \tag{31}$$

in which $\lambda_o = \cos\phi_o$. These may now be substituted into (13) to obtain the field scattered by the loaded parallel plate waveguide. This requires an evaluation of the resulting integrals as

described next.

To compute the field diffracted by the geometry in Figure 3b, (31) is substituted in (13) and a steepest descent path approximation is performed for large kρ. Noting that the pertinent saddle point is at $\alpha = \phi$ when $\phi < \pi$ and at $\alpha = 2\pi - \phi$ when $\phi > \pi$ we find that

$$H_z^s \sim S_{DD}(\phi, \phi_o) \frac{e^{-jk\rho}}{\sqrt{\rho}}$$

where $S_{DD}(\phi, \phi_o)$ is the direct diffraction coefficient given by

$$S_{DD}(\phi, \phi_o) = \frac{-e^{-j\pi/4}}{\sqrt{2\pi k}} \frac{\cos(\phi/2)\cos(\phi_o/2)}{\cos\phi + \cos\phi_o} \begin{Bmatrix} 1 \\ e^{-j2kt\sin\phi} \end{Bmatrix}$$

$$\left\{ \left(1 - R_H + T_H e^{-j2kt\sin\phi_o}\right) \frac{L_1(\cos\phi)\, U_3(\cos\phi_o)}{L_3(\cos\phi)\, U_1(\cos\phi_o)} \pm \left(1 - R_H - T_H e^{-j2kt\sin\phi_o}\right) \frac{L_2(\cos\phi)\, U_4(\cos\phi_o)}{L_4(\cos\phi)\, U_2(\cos\phi_o)} \right\} \tag{32}$$

in which the upper sign holds for $0 < \phi < \pi$ and the lower for $\pi < \phi < 2\pi$.

For the computation of the field coupled into the waveguide (x>0), kρ cannot be assumed large. Therefore, one must employ a technique other than the steepest descent method for its evaluation. A standard procedure is to transform (13b) to the λ-plane giving

$$H_z^s = H_{z2}^s = \frac{\varepsilon_r}{2\pi} \int_{-\infty}^{\infty} \frac{\sqrt{2}\cos(\phi_o/2)\sqrt{1+\lambda}}{\sqrt{\kappa^2 - \lambda^2}\,(\lambda + \lambda_o)} \left\{ \left(1 - R_H + T_H e^{-j2kt\sin\phi_o}\right) \frac{U_3(\lambda_o)}{L_3(\lambda)\, U_1(\lambda)\, U_1(\lambda_o)} \right.$$

$$\left. \sin\left[k(y+t)\sqrt{\kappa^2 - \lambda^2}\right] - j\left(1 - R_H - T_H e^{-j2kt\sin\phi_o}\right) \frac{U_4(\lambda_o)}{L_4(\lambda)\, U_2(\lambda)\, U_2(\lambda_o)} \cos\left[k(y+t)\sqrt{\kappa^2 - \lambda^2}\right] \right\}$$

$$e^{-jkt\sqrt{\kappa^2 - \lambda^2}}\, e^{-jkx\lambda}\, d\lambda \tag{33}$$

where we have defined $\lambda_o = \cos\phi_o$. Since x>0, the above integrals can be evaluated via the residue theorem after closing the path of integration by a semi-infinite contour in the lower half of the λ-plane. In doing this, it should be remarked, that the above integrand does not have a branch at $\lambda = \kappa$. Noting now that $U_{1,2}(\lambda)$ have zeros at

$$\lambda = \lambda_n = \sqrt{\kappa^2 - \left(\frac{n\pi}{2kt}\right)^2} \tag{34}$$

and that

$$U_2(\lambda) = L_2(-\lambda) = \sqrt{2kt}\,\sqrt{\kappa - \lambda}\;U_{2+}(\lambda) \tag{35}$$

we find

$$H_z^s = H_{z2}^s = \sum_{n=0,1,2\ldots}^{\infty} C_n \begin{matrix}\sin\\ \cos\end{matrix}\left[\frac{n\pi}{2t}(y+t)\right] e^{-jkx\lambda_n} \tag{36}$$

where

$$C_{\substack{n_o\\ n_e}}(\phi_o) = -\varepsilon_r \left\{\begin{matrix} j\\ 1\end{matrix}\right\} e^{-j\frac{n\pi}{2}} \left(\frac{2kt}{n\pi}\right) \frac{\sqrt{2}\cos(\phi_o/2)\sqrt{1+\lambda_n}}{\cos\phi_o + \lambda_n}\left(1 - R_H \pm T_H e^{-j2kt\,\sin\phi_o}\right)$$

$$\frac{U_{\substack{3\\4}}(\lambda_o)}{U_1'(\lambda_n)\,U_{\substack{1\\2}}(\lambda_o)\,L_{\substack{3\\4}}(\lambda_n)} \quad ;n \neq 0, \tag{37a}$$

and

$$C_o(\phi_o) = \frac{\varepsilon_r}{2\sqrt{k't}} \frac{\sqrt{2}\cos(\phi_o/2)\sqrt{1+\kappa}}{\cos\phi_o + \kappa}\left(1 - R_H - T_H e^{-j2kt\,\sin\phi_o}\right) \frac{U_4(\lambda_o)}{U_{2+}(\kappa)\,U_2(\lambda_o)\,L_4(\kappa)} \;; n=0$$

(37b)

are the coupling coefficients. In the above, the subscripts $\begin{matrix}o\\ e\end{matrix}$ denote odd and even n, respectively, and

$$U_{\frac{1}{2}}(\lambda_n) = \frac{dU_{\frac{1}{2}}(\lambda)}{d\lambda}\Big|_{\lambda=\lambda_n} .$$

As a check, we note that when $\varepsilon_r = \mu_r = 1$, (32) and (37) reduce to the known expressions given in [12]. In passing, we also note that if we were concerned with the modal fields in the region $x < 0$, we would also have to consider the residues of the poles corresponding to the zeros of $L_{3,4}(\cos\alpha)$. These are precisely the surface wave modes of a dielectric waveguide. Furthermore, any branch-cut contribution would also have to be included.

IV. Radiation and Reflection by a Waveguide Mode

This problem is illustrated by Figures 3d, 3e, and 3f. The modal field (see (36))

$$H^i_{z_o} = \begin{matrix}\sin\\ \cos\end{matrix}\left[\frac{n\pi}{2t}(y+t)\right]e^{jkx\lambda_n} ,$$

$$E^i_{x_o} = \mp j\frac{Z'}{\kappa}\left(\frac{n\pi}{2kt}\right)\begin{matrix}\cos\\ \sin\end{matrix}\left[\frac{n\pi}{2t}(y+t)\right]e^{jkx\lambda_n}$$

is now assumed to be incident toward the waveguide mouth and present throughout the region $-\infty < x < \infty$, $0 > y > -2t$.

Our solution for the radiated field and that reflected back into the waveguide will follow the same general steps employed in the plane wave incidence analysis. The sum of the radiated and reflected fields are now the scattered fields and since they are solely caused by the currents on the perfectly conducting half-plane they can again be represented by (13) - (14). In addition, all of the boundary conditions (B1) - (B6) stated earlier are still valid. Their mathematical forms are now given by

(B1) $E^s_{x1} = E^s_{x2}$ over $-\infty < x < \infty$, $y = 0$,

(B2) $E^s_{x2} = E^s_{x3}$ over $-\infty < x < \infty$, $y = -2t$,

(B3) $H^s_{z1} = H^s_{z2} + H^i_z$ over $x < 0$, $y = 0$,

(B4) $H^s_{z3} = H^s_{z2} + H^i_z$ over $x < 0$, $y = -2t$,

(B5) $E^s_{x1} = 0$ over $x > 0$, $y = 0$,

(B6) $E^s_{x3} = 0$ over $x > 0$, $y = -2t$,

since E^i_x is already zero over the perfectly conducting half-planes.

Application of the boundary conditions (B1) - (B2) again result in the relations given by (17). Thus the determination of $Q_{1,2}(\cos\alpha)$ is our only remaining task. To find these, we proceed with the application of boundary conditions (B3) and (B4), then add and subtract the resulting equations to obtain

$$\int_{-\infty}^{\infty} [\, Q_{1_e^o}(\lambda) + Q_{2_e^o}(\lambda)\,] \frac{\sqrt{\kappa^2 - \lambda^2}}{1 - \lambda^2} L_3(\lambda)\, U_3(\lambda)\, e^{-jkx\lambda}\, d\lambda = \begin{cases} \dfrac{2\varepsilon_r}{\varepsilon_r + 1} \sin\left(\dfrac{n\pi}{2}\right) e^{jkx\,\lambda_n} \\ \\ 0 \end{cases} \quad ; x < 0 \tag{38}$$

$$\int_{-\infty}^{\infty} [\, Q_{1_e^o}(\lambda) - Q_{2_e^o}(\lambda)\,] \frac{\sqrt{\kappa^2 - \lambda^2}}{1 - \lambda^2} L_4(\lambda)\, U_4(\lambda)\, e^{-jkx\lambda}\, d\lambda = \begin{cases} 0 \\ \\ \dfrac{2\varepsilon_r}{\varepsilon_r + 1} \cos\left(\dfrac{n\pi}{2}\right) e^{jkx\,\lambda_n} \end{cases} \quad ; x < 0 \,. \tag{39}$$

By enforcing boundary conditions (B5) - (B6) and again adding and subtracting the resulting equations, we also have that

$$\int_{-\infty}^{\infty} [\, Q_{1_{o\,e}}(\lambda) + Q_{2_{o\,e}}(\lambda)\,] \frac{\sqrt{\kappa^2 - \lambda^2}}{\sqrt{1-\lambda^2}} L_1(\lambda)\, U_1(\lambda)\, e^{-jkx\lambda}\, d\lambda = 0 \quad ; x > 0 \quad , \tag{40}$$

$$\int_{-\infty}^{\infty} [\, Q_{1_{o\,e}}(\lambda) - Q_{2_{o\,e}}(\lambda)\,] \frac{\sqrt{\kappa^2 - \lambda^2}}{\sqrt{1-\lambda^2}} L_2(\lambda)\, U_2(\lambda)\, e^{-jkx\lambda}\, d\lambda = 0 \quad ; x > 0 \quad . \tag{41}$$

Equations (38) with (40) and (39) with (41) form again a coupled set sufficient for the solution of $Q_{1,2}(\lambda)$. In proceeding with this solution, we note that since (40) - (41) are valid for $x > 0$, the path of integration may be closed by a semi-infinite contour in the lower half of the λ-plane, giving

$$[\, Q_{1_{o\,e}}(\lambda) + Q_{2_{o\,e}}(\lambda)\,] \frac{\sqrt{\kappa^2 - \lambda^2}}{\sqrt{1-\lambda^2}} L_1(\lambda)\, U_1(\lambda) = L_{A_{o\,e}}(\lambda) \quad , \tag{42}$$

$$[\, Q_{1_{o\,e}}(\lambda) - Q_{2_{o\,e}}(\lambda)\,] \frac{\sqrt{\kappa^2 - \lambda^2}}{\sqrt{1-\lambda^2}} L_2(\lambda)\, U_2(\lambda) = L_{B_{o\,e}}(\lambda) \tag{43}$$

where $L_A(\lambda)$ and $L_B(\lambda)$ are again unknown functions regular in the lower half λ-plane. Similarly, because (38) - (39) apply to $x < 0$, we may close the path of integration with a semi-infinite contour in the upper half of the λ-plane resulting to

$$[\,Q_{1_{e}^{o}}(\lambda) + Q_{2_{e}^{o}}(\lambda)\,]\frac{\sqrt{\kappa^2-\lambda^2}}{1-\lambda^2}L_3(\lambda)\,U_3(\lambda) = \begin{cases} \dfrac{\varepsilon_r}{(\varepsilon_r+1)\,\pi j}\dfrac{\sin(\frac{n\pi}{2})}{\lambda+\lambda_n}\dfrac{U_{A_o}(\lambda)}{U_{A_o}(-\lambda_n)} \\ U_{A_e}(\lambda)\,E_A(\lambda) \end{cases} \tag{44}$$

$$[\,Q_{1_{e}^{o}}(\lambda) - Q_{2_{e}^{o}}(\lambda)\,]\frac{\sqrt{\kappa^2-\lambda^2}}{1-\lambda^2}L_4(\lambda)\,U_4(\lambda) = \begin{cases} U_{B_o}(\lambda)\,E_B(\lambda) \\ \dfrac{\varepsilon_r}{(\varepsilon_r+1)\,\pi j}\dfrac{\cos(\frac{n\pi}{2})}{\lambda+\lambda_n}\dfrac{U_{B_e}(\lambda)}{U_{B_e}(-\lambda_n)} \end{cases} \tag{45}$$

where U_A , U_B are unknown functions regular in the upper half of the λ-plane and $E_{A,B}(\lambda)$ are unknown entire functions whose justification for the appearance of will soon become apparent. Substituting (42), (43) into (44), (45) respectively, and equating regions of regularity we find

$$U_{A_{e}^{o}}(\lambda) = U_A(\lambda) = \frac{U_3(\lambda)}{\sqrt{1-\lambda}\;U_1(\lambda)}\quad , \tag{46a}$$

$$U_{B_{e}^{o}}(\lambda) = U_B(\lambda) = \frac{U_4(\lambda)}{\sqrt{1-\lambda}\;U_2(\lambda)}\quad , \tag{46b}$$

$$L_{A_{e}^{o}}(\lambda) = \begin{cases} \dfrac{\varepsilon_r \sin(\frac{n\pi}{2})}{(\varepsilon_r+1)\,\pi j}\dfrac{\sqrt{1+\lambda}\;\sqrt{1+\lambda_n}}{\lambda+\lambda_n}\dfrac{L_1(\lambda)\,L_1(\lambda_n)}{L_3(\lambda)\,L_3(\lambda_n)} \\ \dfrac{\sqrt{1+\lambda}\;L_1(\lambda)}{L_3(\lambda)}E_A(\lambda)\quad , \end{cases} \tag{46c}$$

$$L_{B_{o_e}}(\lambda) = \begin{cases} \dfrac{\sqrt{1+\lambda}\; L_2(\lambda)}{L_4(\lambda)} E_B(\lambda) \\ \dfrac{\varepsilon_r \cos\left(\frac{n\pi}{2}\right)}{(\varepsilon_r+1)\,\pi j} \dfrac{\sqrt{1+\lambda}\,\sqrt{1+\lambda_n}}{\lambda+\lambda_n} \dfrac{L_2(\lambda)\,L_2(\lambda_n)}{L_4(\lambda)\,L_4(\lambda_n)} \end{cases} . \tag{46d}$$

We may now use (17), (44), (45), and (46) to determine the spectra $P_{1,2}(\lambda)$ as

$$P_{1_{o_e}}(\lambda) = \frac{\sqrt{1+\lambda}\; L_{2_1}(\lambda)}{2\varepsilon_r L_{4_3}(\lambda)} E_{B_A}(\lambda) + \frac{\sin\left(\frac{n\pi}{2}\right)}{\cos(\varepsilon_r+1)\,2\pi j} \frac{\sqrt{1+\lambda_n}\,\sqrt{1+\lambda}}{\lambda+\lambda_n} \frac{L_{1_2}(\lambda)\,L_{1_2}(\lambda_n)}{L_{3_4}(\lambda)\,L_{3_4}(\lambda_n)} , \tag{47}$$

$$P_{2_{o_e}}(\lambda) = \mp \frac{\sqrt{1+\lambda}\; L_{2_1}(\lambda)}{2\varepsilon_r L_{4_3}(\lambda)} E_{B_A}(\lambda) \pm \frac{\sin\left(\frac{n\pi}{2}\right)}{\cos(\varepsilon_r+1)\,2\pi j} \frac{\sqrt{1+\lambda}\,\sqrt{1+\lambda_n}}{\lambda+\lambda_n} \frac{L_{1_2}(\lambda)\,L_{1_2}(\lambda_n)}{L_{3_4}(\lambda)\,L_{3_4}(\lambda_n)} , \tag{48}$$

with the evaluation of $E_A(\lambda)$ and $E_B(\lambda)$ remaining. From a straight forward examination of the field behavior at the plate edges, it can be shown that [13] $P(\lambda) \sim \lambda^{-1/2}$ as $\mathrm{Re}(\lambda) \to \infty$ and since $L_{1,2}(\lambda)$, $L_{3,4}(\lambda) \to 1$ as $\mathrm{Re}(\lambda) \to \infty$, one concludes that

$$E_A(\lambda) = E_B(\lambda) = 0 . \tag{49}$$

Consequently, we find that

$$P_{1_{o_e}}(\lambda) = \pm P_{2_{o_e}}(\lambda) = \frac{\sin(\frac{n\pi}{2})}{\cos(\frac{n\pi}{2})} \frac{\sqrt{1+\lambda}\sqrt{1+\lambda_n}}{(\varepsilon_r+1)\,2\pi j} \frac{L_{\frac{1}{2}}(\lambda)\,L_{\frac{1}{2}}(\lambda_n)}{\lambda+\lambda_n} \frac{}{L_{\frac{3}{4}}(\lambda)\,L_{\frac{3}{4}}(\lambda_n)}, \tag{50}$$

$$Q_{1_{o_e}}(\lambda) = \pm Q_{2_{o_e}}(\lambda) = \frac{\sqrt{1-\lambda^2}}{\sqrt{\kappa^2-\lambda^2}} \frac{\varepsilon_r \sin(\frac{n\pi}{2})}{\cos(\frac{n\pi}{2})} \frac{\sqrt{1+\lambda}\sqrt{1+\lambda_n}}{(\varepsilon_r+1)\,2\pi j} \frac{L_{\frac{1}{2}}(\lambda_n)}{\lambda+\lambda_n} \frac{}{U_{1_{2}}(\lambda)\,L_{\frac{3}{4}}(\lambda)\,L_{\frac{3}{4}}(\lambda_n)}. \tag{51}$$

The radiated field is now found by substituting (50) into (13). After employing a steepest descent path evaluation of the resulting integrals for large kρ we obtain

$$H^s_{z_{o_e}} = \begin{cases} H^s_{z1_{o_e}}; & 0<\phi<\pi \\ H^s_{z3_{o_e}}; & \pi<\phi<2\pi \end{cases} \sim \frac{e^{-jk\rho}}{\sqrt{\rho}} L_{n_{o_e}}(\phi) \tag{52}$$

where the launching coefficients $L_{n_{o_e}}(\phi)$ are given by

$$L_{n_{o_e}} = \begin{cases} A\sin\frac{n\pi}{2} \\ B\cos\frac{n\pi}{2} \end{cases} \frac{e^{-j\pi/4}}{\sqrt{2\pi k}\,(\varepsilon_r+1)} \frac{\sqrt{2}\cos\phi/2\sqrt{1+\lambda_n}}{\cos\phi+\lambda_n} \frac{L_{1_{2}}(\cos\phi)L_{1_{2}}(\lambda_n)}{L_{3_{4}}(\cos\phi)L_{3_{4}}(\lambda_n)} \tag{53}$$

in which A = B = 1 when $0<\phi<\pi$ and $A = e^{-j2kt\sin\phi}$, $B = -e^{-j2kt\sin\phi}$ when $\pi<\phi<2\pi$.

The field reflected back into the waveguide is H^s_{z2} in (13) and is evaluated by the same procedure employed for the coupled field. Specifically, we transform the integration path to the λ-plane and invoke Cauchy's theorem after closing the path of integration with a semi-infinite circle in the lower half of the λ-plane to obtain

$$H^s_{z_{o_e}} = H^s_{z2_{o_e}} = \sum_{m=0,1,2} R_{m_o n_o \atop e\ e} \begin{matrix}\sin\\ \cos\end{matrix}\left[\frac{m\pi}{2t}(y+t)\right] e^{-jkx\lambda_m} \tag{54}$$

where

$$R_{m_o n_o \atop e\ e} = \frac{4\varepsilon_r kt \begin{Bmatrix} j \\ 1 \end{Bmatrix} \begin{matrix}\sin\\ \cos\end{matrix}(\frac{m\pi}{2})}{m\pi(\varepsilon_r+1)} \frac{\sqrt{1+\lambda_m}\sqrt{1+\lambda_n}}{\lambda_n+\lambda_m} \frac{L_{\frac{1}{2}}(\lambda_n)}{U'_{\frac{1}{2}}(\lambda_m) L_{\frac{3}{4}}(\lambda_m) L_{\frac{3}{4}}(\lambda_n)} e^{-j\frac{m\pi}{2}} \quad ; m \neq 0 \ , \tag{55a}$$

$$R_{o_n \atop e} = \frac{-\varepsilon_r}{\sqrt{\kappa' t}\,(\varepsilon_r+1)} \frac{\sqrt{1+\kappa}\sqrt{1+\lambda_n}}{\kappa+\lambda_n} \frac{L_2(\lambda_n)}{U_{2+}(\kappa) L_4(\kappa) L_4(\lambda_n)} \quad ; m=0 \ , \tag{55b}$$

$$R_{m_o n_e} = R_{m_e n_o} = 0 \tag{55c}$$

are the reflection coefficients.

Finally, the matrix elements Γ_{mn} due to reflection from a perfectly conducting slab are given for the H_z-polarization by

$$\Gamma_{mn} = \begin{cases} 1, & m=n, \\ 0, & m \neq n, \end{cases} \tag{56}$$

implying that $[\Gamma_{mn}]$ is the identity matrix.

This completes the analysis required for the evaluation of the diffracted field H^s_z by the thick metallic-dielectric join shown in Figure 1. Below we present some numerical data which describe the scattering behavior of the metallic-dielectric join as function of thickness and the dielectric's constitutive parameters.

V. Numerical Results

Before proceeding with the computation of the diffracted field by the join as given in (1), it is essential to first determine the minimum number of modes required to achieve convergence of the infinite sum implied in (4). Such a convergence test was also done in [12] where the special case of $\varepsilon_r = \mu_r = 1$ was considered, and was found that only a few evanescent modes in addition to the propagating ones were required to obtain sufficient computational accuracy. Unfortunately, as will be seen, the presence of the dielectric slab complicates this issue and it is therefore necessary that we examine the convergence of the solution as a function of the constitutive parameters of the slab. Further, we will limit our interest to slab thickness less than a wavelength.

The convergence of the solution (1) is examined in Figure 7 where backscatter curves are given for a metallic-dielectric join 0.95 wavelengths thick and for three separate sets of values for ε_r , μ_r . As seen, for the case of $\varepsilon_r = 2$, $\mu_r = 1$ at least twelve modes are required to achieve convergence whereas, as noted in [12], for the case of no dielectric, five modes were required. This is probably due to stronger diffractions from the lower dielectric-metallic junction. However, as expected and shown in Figures 7b - 7c, when some loss is introduced in the dielectric, convergence can be achieved with less modes.

Now that the convergence of the solution (1) has been examined, we can proceed with the calculation of the scattering by the metallic-dielectric join shown in Figure 1. In figures 8-10 we present a sequence of echowidth curves corresponding to three different sets of (ε_r , μ_r) and various join thicknesses from 0.01 to 0.75 wavelengths. Each figure includes a family of curves for five thicknesses in the range $0.01\lambda < 2t < 0.75\lambda$ computed for the backscatter case and two bistatic situations with $\phi_0 = 45°$ and $\phi_0 = 150°$. Unfortunately, no

comparison with an alternate solution can be provided for any of the presented curves since to our knowledge an alternative solution does not exist.

SUMMARY

The dual integral equation approach along with the generalized scattering matrix formulation were employed for the diffraction analysis of a thick dielectric-metallic join with H-polarization of incidence. To obtain the solution for diffracted field by the join we first considered the problem of an open-ended waveguide loaded with an extended dielectric slab and containing a recessed stub as shown in Figure 3a. Before proceeding with the application of the scattering matrix formulation, the problems of 1) direct diffraction and coupling due to a plane wave incidence and 2) radiation and reflection by a waveguide mode were first considered. For each of the above problems the pertinent fields were first expressed in terms of the plane wave spectra corresponding to the currents on the surface of the half-planes forming the waveguide. The application of the boundary conditions then allowed us to find explicit expressions for the current spectra after first decoupling the resulting dual integral equations and subsequently employing an asymptotic or residue series evaluation of the pertinent integrals. Implicit in this analysis is the Wiener-Hopf factorization of several functions and in some cases this was accomplished via numerical means using a new technique described in Appendix B.

At the end of the paper, several backscatter and bistatic calculated echowidth patterns are given for $0.01\lambda < 2t < 0.75\lambda$ corresponding to three sets of constitutive parameters for the dielectric. In addition, a few curves are given which describe the convergence of the solution as a function of the number of included modes.

FIGURES

REFERENCES

1. C.M. Angulo and W.S. Chang, "The Launching of Surface Waves by a Parallel Plate Waveguide," IRE Transcations on Antennas and Propagation, Vol. AP-7, pp. 359-368, October 1959.

2. C.P. Bates and R. Mittra, "Waveguide Excitation of Dielectric and Plasma Slabs," Radio Science, Vol. 3, No. 3, pp. 251-266, March 1968.

3. K. Uchida and K. Aoki, "Radiation From and Surface Wave Excitation by an Open-Ended Dielectric-Loaded Parallel-Plate Waveguide," The Transactions of the IECE of Japan, Vol. E-67, No. 4, pp. 218-224, April 1984.

4. D.C. Chang and E.F. Kuester, "Total and Partial Reflection From the End of a Parallel-Plate Waveguide With an Extended Dielectric Slab," Radio Science, Vol. 16, No. 1, pp. 1-13, January-February 1981.

5. T.T. Fong, "Radiation From an Open-Ended Waveguide With Extended Dielectric Loading," Radio Science, Vol. 7, No. 10, pp. 965-972, October 1972.

6. P.H. Pathak and R.G. Kouyoumjian, "Surface Wave Diffraction by a Truncated Dielectric Slab Recessed in a Perfectly Conducting Surface," Radio Science, Vol. 14, No. 3, pp. 405-417, May-June 1979.

7. K. Aoki and K. Uchida, "Scattering of a Plane Electromagnetic Wave by Two Semi-Infinite Dielectric Slabs," The Transactions of the IECE of Japan, Vol. 62-B, No. 12, pp. 1132-1139, 1979.

8. J.R. Pace and R. Mittra, "Generalized Scattering Matrix Analysis of Waveguide Discontinuity Problems," Proc. Symp. Quasi-Optics, Vol. 14, Brooklyn, N.Y., Polytechnic Inst. of Brooklyn Press, pp. 177-197, 1964.

9. P.C. Clemmow, "A Method for the Exact Solution of a Class of Two-Dimensional Diffraction Problems," Proc. Roy Soc. A., Vol. 205, pp. 286-308, 1951.

10. S.W. Lee and R. Mittra, "Diffraction by Thick Conducting Half-Plane and a Dielectric-Loaded Waveguide," IEEE Transactions on Antennas and Propagation, Vol. AP-16, No. 4, pp. 454-461, July 1968.

11. B. Noble, Methods Based on the Wiener-Hopf Technique, Chapter 1, Pergamon, 1958.

12. J.L. Volakis and M.A. Ricoy, "Diffraction by a Thick Conducting Half-Plane," IEEE Transactions on Antennas and Propagation, Vol. AP-35, pp. 62-72, January 1987.

13. R. Mittra and S.W. Lee, Analytical Techniques in the Theory of Guided Waves, pp. 4-11, MacMillan, 1971.

14. R.D. Coblin, "Scattering of an Electromagnetic Plane Wave From a Perfectly Electrically Conducting Half-Plane in the Proximity of Planar Media Discontinuities," Ph.D. dissertation, Univ. of Mississippi, 1983, pp. 122-129.

Appendix A

Expressions for the Split Functions $L_{1,2}(\lambda)$ and $U_{1,2}(\lambda)$

The split functions $U_2(\lambda)$ and $L_2(\lambda)$ arise in the factorization of the functions $(1 \pm e^{-j2kt\sqrt{\kappa^2-\lambda^2}})$ as follows:

$$1 \pm e^{-j2kt\sqrt{\kappa^2 - \lambda^2}} = U_2(\lambda)\, L_2(\lambda) \ . \tag{A1}$$

The U functions are free of branch cuts, poles and zeros (i.e., regular) in the upper half of the λ-plane shown in Fig. 6. Similarly the L functions are regular in the lower half of the λ-plane.

These functions may be derived using the procedure given by Noble [11]. The appropriate expressions for the $e^{j\omega t}$ convention employed in this paper are

$$U_1(\lambda) = L_1(-\lambda) = \sqrt{2}\exp[-T(\lambda)-X_1(\lambda)] \prod_{n=1,3,5\ldots}^{\infty} \left(\frac{-j2kt}{n\pi}\right)(\lambda-\lambda_n)\exp(j2kt\lambda/n\pi) \ , \tag{A2}$$

$$U_2(\lambda) = L_2(-\lambda) = e^{j\pi/4}\sqrt{2kt}\sqrt{\kappa-\lambda}\exp[-T(\lambda)-X_2(\lambda)] \prod_{n=2,4,6\ \ldots}^{\infty} \left(\frac{-j2kt}{n\pi}\right)(\lambda-\lambda_n)\exp(j2kt\lambda/n\pi) \tag{A3}$$

where

$$T(\lambda) = -jkt\sqrt{\kappa^2-\lambda^2}\left[1 - \frac{\cos^{-1}(\lambda/\kappa)}{\pi}\right] \ , \tag{A4}$$

$$X_2(\lambda) = \frac{j\lambda kt}{\pi}\left[0.4228 + \ln\left(\frac{\pi}{k't}\right) \mp \ln 2\right] + \frac{kt\lambda}{2} \qquad \text{(A5)}$$

and

$$\lambda_n = \sqrt{\kappa^2 - \left(\frac{n\pi}{2kt}\right)^2} \quad . \qquad \text{(A6)}$$

The branch of the logarithm appearing in the above function is that of $-\pi \leq \mathrm{Im}(\ln) < \pi$, while all remaining branches are explicitly defined in Figures 4, 5, and 6.

Appendix B

An Efficient Numerical Wiener-Hopf Factorization Method

A crucial and major step in obtaining a solution to a Weiner-Hopf equation is the factorization/splitting of an even function $F(\alpha)$ into a product of two functions such that

$$F(\alpha) = L(\alpha)\, U(\alpha) \tag{B1}$$

where $\alpha = \sigma + j\tau$. In the above, $U(\alpha)$ is free of zeros, poles and branch cuts (i.e., regular) in the upper half of the α-plane ($\tau > \tau_-$) shown in Figure B1, while $L(\alpha)$ is regular in the lower half of the α-plane ($\tau < \tau_+$), where $\tau_- < \tau_+$. To accomplish the factorization (B1) we must generally assume that $F(\alpha)$ is regular within the strip $\tau_- < \tau < \tau_+$, where $\tau_\pm$ are allowed to approach vanishing values. If we further demand that $F(\alpha) \to 1$ uniformly as $|\sigma| \to \infty$ within the strip, then $U(\alpha)$ and $L(\alpha)$ are formally given by [13]

$$U(\alpha) = L(-\alpha) = \exp[H(\alpha)]\ ,\ \mathrm{Im}(\alpha) > 0 \tag{B2}$$

where

$$H(\alpha) = \frac{1}{2\pi j} \int_{C_1} \frac{\ln[F(\beta)]}{\beta - \alpha} d\beta \tag{B3}$$

with C_1 as shown in Figure B1. Note, however, that this last condition on $F(\alpha)$ does not necessarily restrict its form since any $F(\alpha)$ can be modified as such in a recoverable manner. Additionally, due to the even property of $F(\alpha)$, we may set $\tau_- = -\tau_+$ implying that the contour

C_1 ($\tau = 0$) remains within the strip $|\tau| < \tau_+$ as $\tau_\pm$ become arbitrarily small.

Despite its general applicability, (B2) contains several barriers to its direct numerical implementation. In addition to displaying infinite limits of integration, the contour integral possesses an integrand which may become singular depending on the contour's location. Further, care must be exercised to insure that a proper branch of the logarithm is taken so that $\ln[F(\beta)]$ is continuous on C_1. Under certain circumstances, however, these problems can be largely alleviated via appropriate modification of (B2).

To this end, suppose that in addition to being regular in the strip $|\tau| < \tau_+$, $F(\beta)$ is also regular in the angular sector $\{\beta(t) = te^{j\theta} ; 0 < \theta < \theta_0 , 0 < t < \infty\}$ for some θ_0 and $F(\beta(t)) \rightarrow 1$ uniformly as $t \rightarrow \infty$ throughout the above sector. Since $F(\beta)$ is even, this also implies it will have the same properties in the additional angular sector $\{\beta(t) = te^{j\theta} ; \pi < \theta < \pi+\theta_0 , 0 < t < \infty\}$. Further, it should be noted that in general most functions requiring factorization in diffraction theory are of this type and, therefore, this is not a significant restriction on $F(\alpha)$. With the above provisions on the regularity of $F(\beta)$, it follows that C_1 can be rotated counter-clockwise about the origin by an angle $\theta(0 < \theta < \theta_0)$ to contour C_2, as shown in Figure B2. $H(\alpha)$ is thus modified a

$$H(\alpha) = h(\theta - \theta_\alpha) \ln[F(\alpha)] + \frac{1}{2\pi j} \int_{C_2} \frac{\ln[F(\beta)]}{\beta - \alpha} d\beta \ , \tag{B3}$$

where

$$h(\theta - \theta_\alpha) = \begin{cases} 0 \text{ for } \theta < \theta_\alpha \ , \\ 1 \text{ for } \theta > \theta_\alpha \ , \end{cases} \tag{B4}$$

and

$$\theta_\alpha = \arctan\left[\frac{\mathrm{Im}(\alpha)}{\mathrm{Re}(\alpha)}\right] . \qquad \text{(B5)}$$

Addressing the singularities associated with the integrand of (B3), it is clear that the numerator becomes infinite when $\beta = \beta_n$, where β_n,n = 1,2, ...N are the N zeros of $F(\beta)$. By virtue of the stipulated regularity of $F(\beta)$ in the angular sectors defined above, β_n are, however, precluded from lying upon the contour C_2. Nevertheless, as θ approaches 0 or θ_0, it is possible for any of the β_n to become arbitrarily close to C_2 (for $\theta \rightarrow 0$, this is true if $\tau_\pm$ tend to zero, which is often the case). Fortunately, the resulting singularity is logarithmic, implying that it need be removed only a small distance from the contour C_2 to substantially reduce the singularity of the integrand. The obvious solution, therefore, is to restrict the permissible angular variation to $\delta_1 < \theta < \theta_0 - \delta_2$, where $\delta_{1,2}$ are small angles which may be determined empirically. This scheme will work provided β_n are not in the vicinity of the origin which prevents the contour in being distanced from the pertinent β_n via a simple rotation.

In contrast to the numerator which may display a multitude of singularities, the denominator contains a single zero at $\beta = \alpha$. Recall that the only condition on α is that $\mathrm{Im}(\alpha) > 0$, admitting the possibility of α lying close to or upon C_2. The simplest method to prevent this is to again impose restrictions on θ, so that $\theta \notin [\theta_\alpha + \varepsilon, \theta_\alpha - \varepsilon]$, where $\theta_\alpha = \arctan\left[\frac{\mathrm{Im}(\alpha)}{\mathrm{Re}(\alpha)}\right]$ and ε is a small angle to be determined empirically. However, the involved singularity is of higher-order than the one previously encountered, implying that $\varepsilon >> \delta$. This greatly restricts the permitted range of θ if $0 < \theta_\alpha < \theta_0$, and is undesirable since the quantity $\ln[F(\beta)]$ may exhibit different rates of convergence as $\beta(t) \rightarrow \infty$ among the admissible θ. One would therefore prefer to

choose an optimum path C_2 from the standpoint of numerical accuracy. Hence, it is of interest to reduce the restricted range $[\theta_\alpha + \varepsilon , \theta_\alpha - \varepsilon]$ so that the likelihood of this range superimposing itself upon a region of optimum convergence is minimized. An appropriate modification to (B3) for accomplishing this is considered next.

The integral in (B3) is obviously not convenient for numerical implementation and it is therefore necessary to rewrite it for that purpose. By introducing the substitution $\beta = te^{j\theta}$ along with the even property of $F(\beta)$ we obtain

$$H(\alpha) = h(\theta - \theta_\alpha)\ln[F(\alpha)] + \frac{\alpha e^{j\theta}}{\pi j} \int_0^\infty \frac{\ln[F(te^{j\theta})]}{t^2 e^{j2\theta} - a^2}\, dt \ . \qquad \text{(B6)}$$

which presents a numerical difficulty when the pole at $t = \alpha e^{-j\theta}$ is near the real axis. This can be treated via an addition-subtraction process, provided $\alpha \notin C_2$. Specifically, we add and subtract to the numerator its value at $t = \alpha e^{-j\theta}$. By evaluating the additive term analytically, (B6) becomes

$$H(\alpha) = \frac{1}{2}\ln[F(\alpha)] + \frac{a e^{j\theta}}{\pi j} \int_0^\infty \frac{\ln[F(te^{j\theta})] - \ln[F(\alpha)]}{t^2 e^{j2\theta} - \alpha^2}\, dt \ , \qquad \text{(B7)}$$

where the integrand is now regular at $t = \alpha e^{-j\theta}$. This effectively reduces ε to the order of δ , increasing the range of allowed θ and thus eliminating the concerns noted in the previous paragraph.

A final obstacle to the numerical evaluation of $H(\alpha)$ is the infinite upper integration limit of (B7). This may be remedied via the change of variables [14] $v = \frac{2}{\pi} \arctan t$ to obtain

$$H(\alpha) = \frac{1}{2}\ln[F(\alpha)] + \frac{\alpha e^{j\theta}}{2j}\int_0^1 \frac{\ln\left[F\left\{e^{j\theta}\tan\left(\frac{\pi v}{2}\right)\right\}\right] - \ln[F(\alpha)]}{\sin^2\left(\frac{\pi v}{2}\right)e^{j2\theta} - \alpha^2\cos^2\left(\frac{\pi v}{2}\right)}\,dv \quad . \tag{B8}$$

The integral can now be easily evaluated especially if θ is chosen such that F(v) exhibits a rapid decay as it increases from 0 to 1.

Expressions (B2) along with (B8) provide a complete prescription for factorizing an even function regular on the strip $|\tau| < \tau_+$ and the angular sectors $0 < \theta < \theta_0$, $\pi < \theta < \pi + \theta_0$. The integral in (B8) is over a convenient finite interval, and will be numerically tractable for $\delta_1 < \theta < \theta_0 < \delta_2$, provided $\theta \notin [\theta_\alpha + \varepsilon, \theta_\alpha - \varepsilon]$ if $0 < \theta_\alpha < \theta_0$ and the zeros of $F(\beta)$ are not too close the origin. This allows a selection of θ such that the numerical accuracy of (B2) and (B6) is optimized. Additionally, care must be taken in defining the branch of the logarithm in (B8) so that $\ln\left[F\left\{e^{j\theta}\tan\left(\frac{\pi v}{2}\right)\right\}\right]$ remains continuous on the path of integration, eliminating a branch cut contribution.

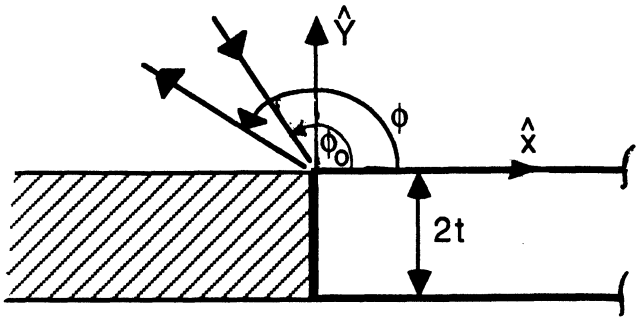

Fig. 1. Geometry of the metallic-dielectric join.

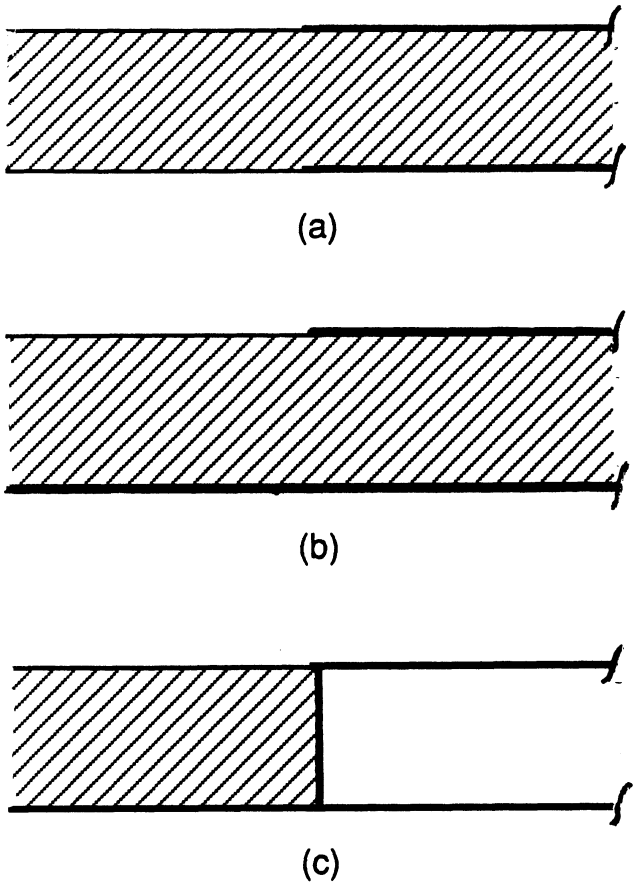

g.2. Structures related to the metallic-dielectric join.
(a) Truncated parallel plate waveguide with extended dielectric loading.
(b) Grounded dielectric slab with truncated upper plate.
(c) Material slab recessed in perfectly conducting half-plane.

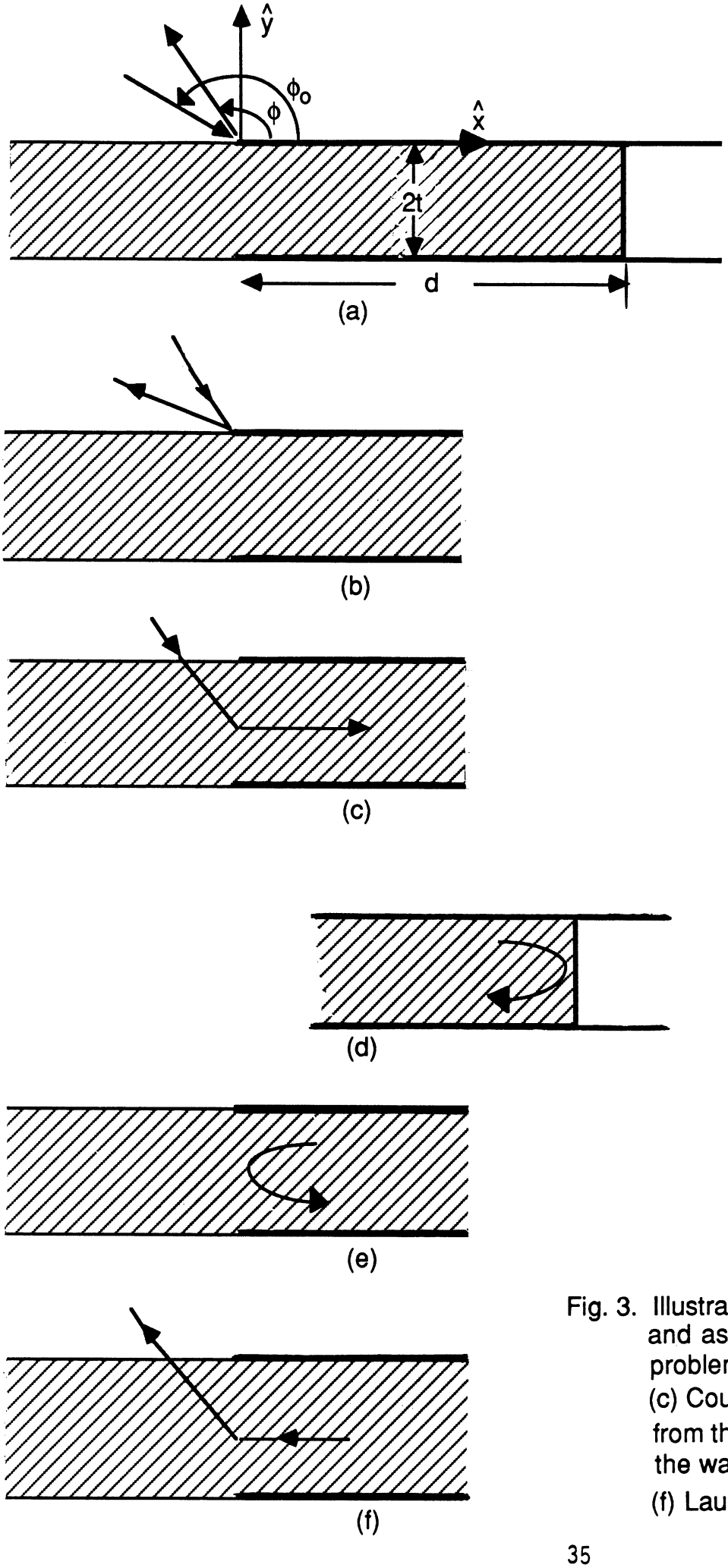

Fig. 3. Illustration of stub geometry (a) and associated individual problems: (b) Direct diffraction. (c) Coupling. (d) Reflection from the stub. (e) Reflection at the waveguide mouth. (f) Launching or radiation.

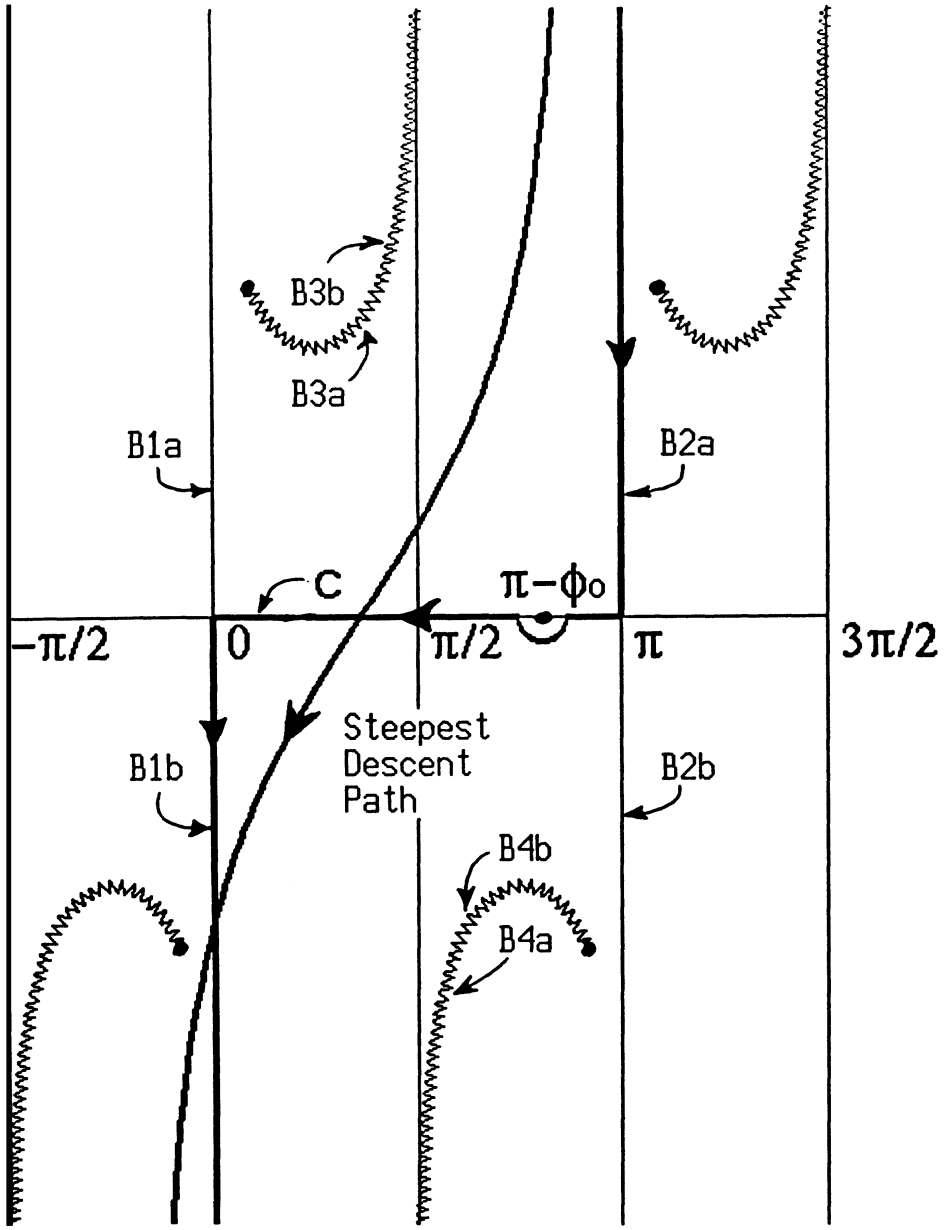

Fig. 4. Illustration of the C and steepest decent path contours in the α-plane along with the chosen branches for the roots sqrt(κ-α) and sqrt(κ+α).

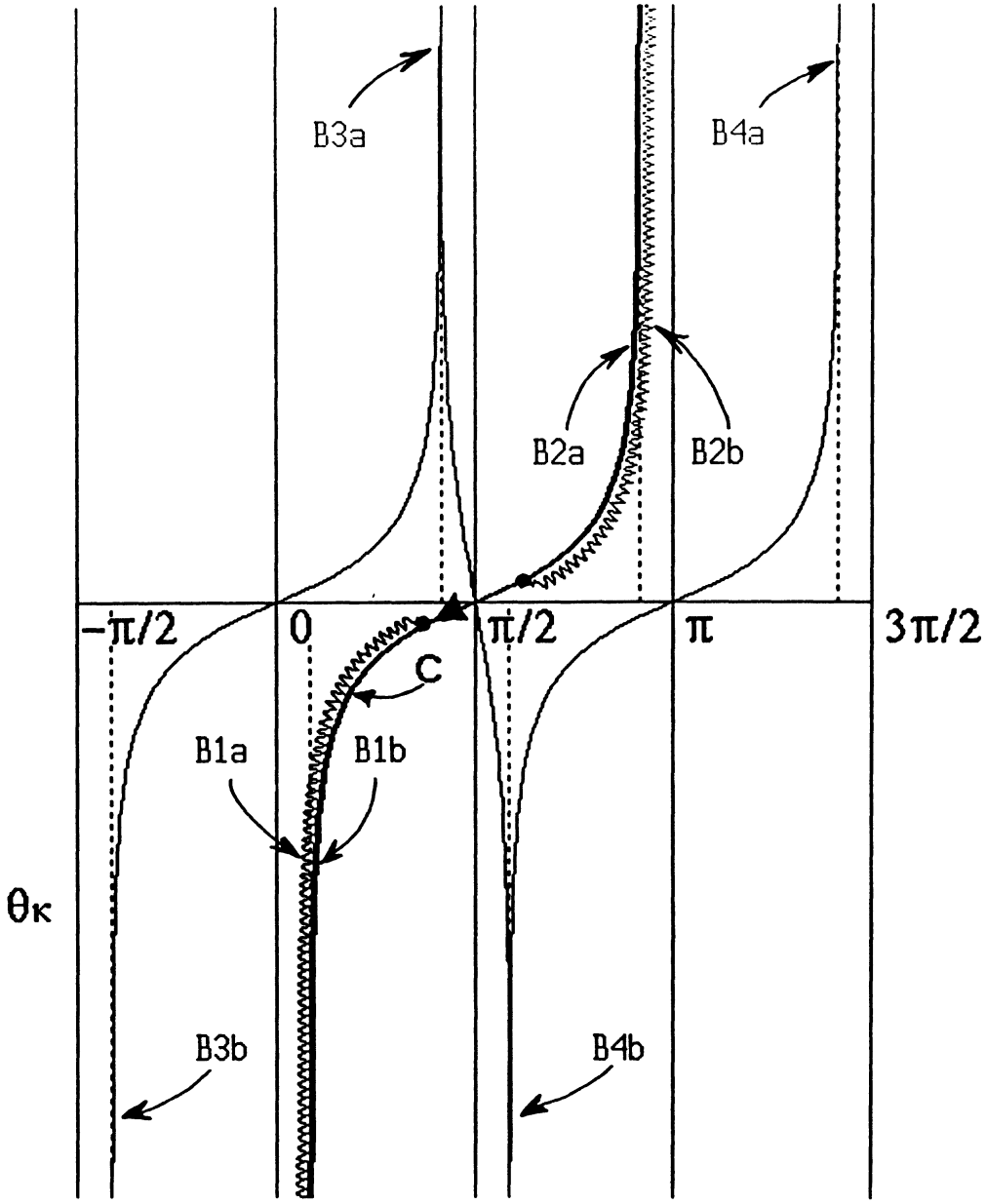

Fig. 5. Mapping of the contours shown in Fig. 3 in the α'-plane, where cosα=κcosα'.

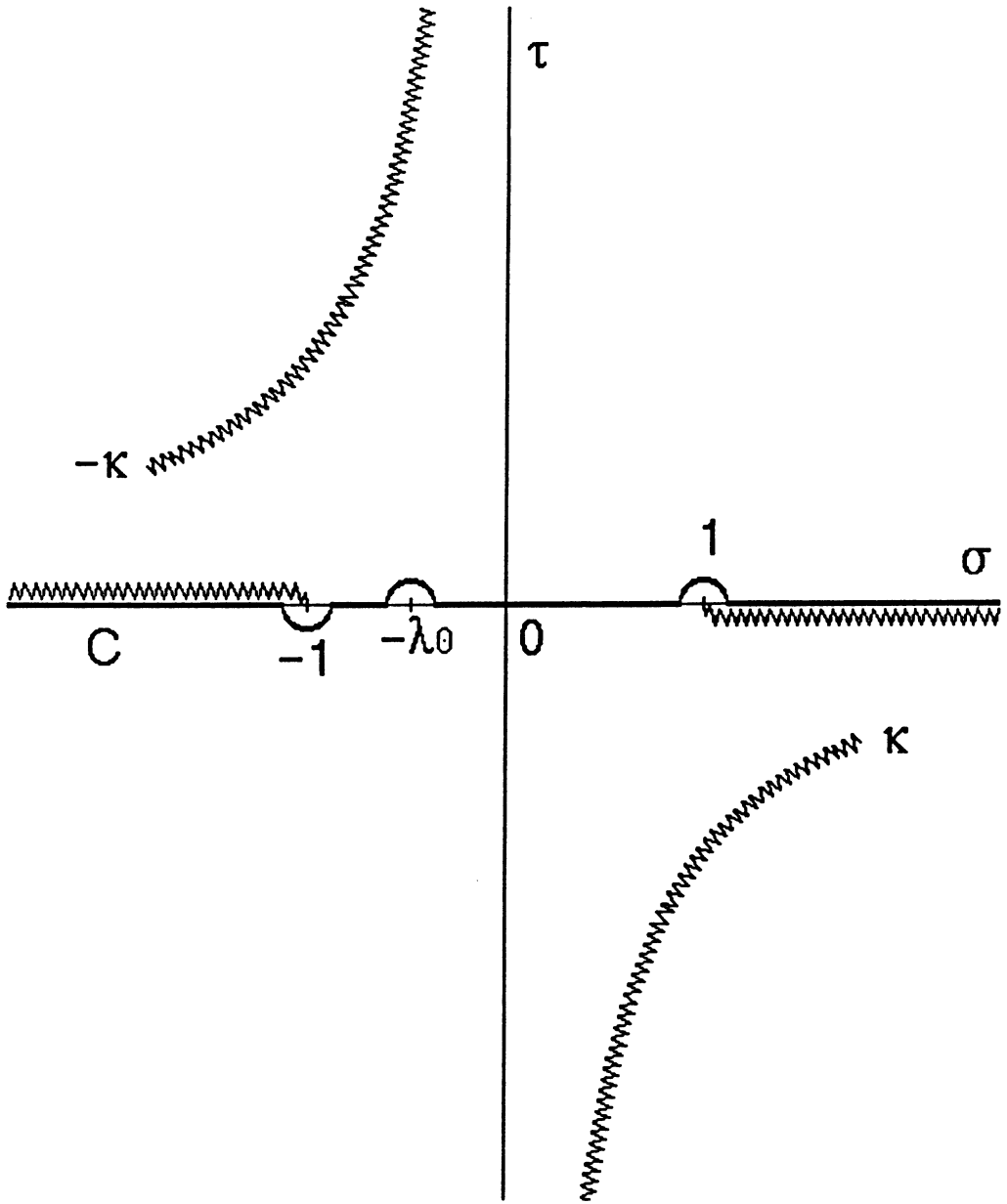

Fig. 6. Illustration of the C contour in the λ-plane, where λ=cosα.

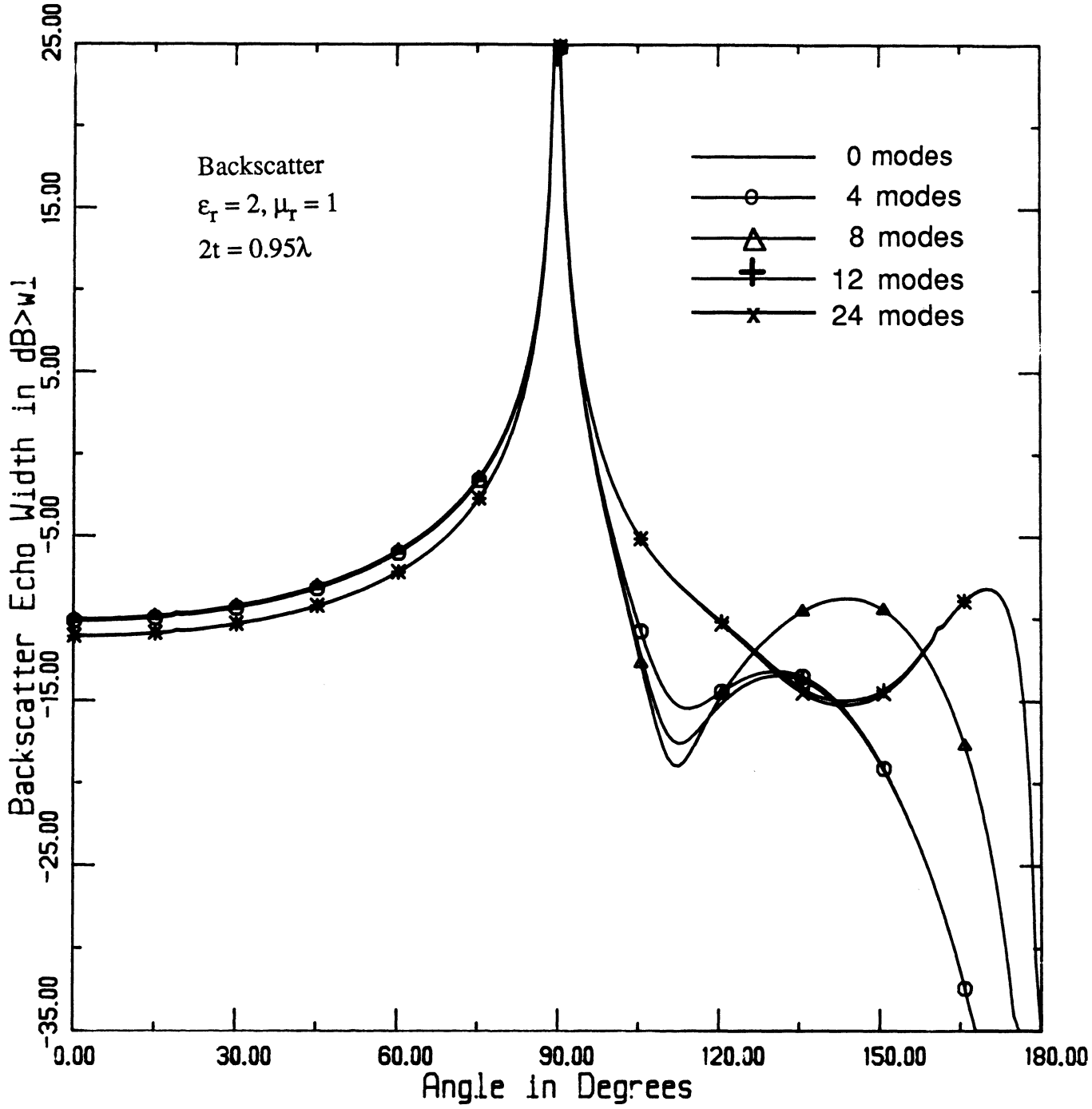

(a)

Fig. 7. Convergence test of the solution given in equation (1).

(a) $2t = 0.95\lambda$, $\varepsilon_r = 2$, $\mu_r = 1$

(b) $2t = 0.95\lambda$, $\varepsilon_r = 5 - j0.5$, $\mu_r = 1.5 - j0.1$

(c) $2t = 0.95\lambda$, $\varepsilon_r = 7.4 - j1.1$, $\mu_r = 1.4 - j0.672$

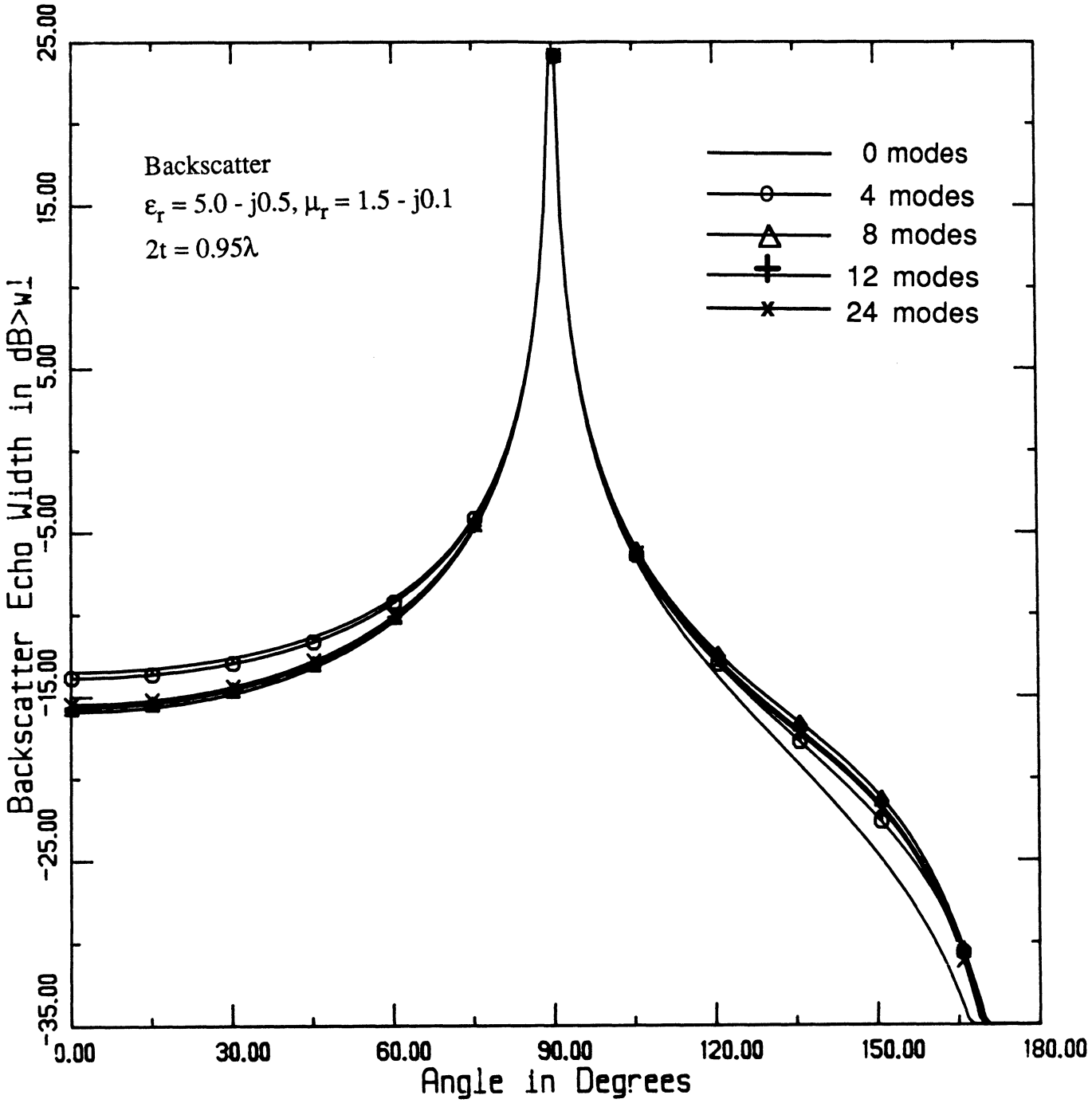
Backscatter
$\varepsilon_r = 5.0 - j0.5, \mu_r = 1.5 - j0.1$
$2t = 0.95\lambda$
0 modes
4 modes
8 modes
12 modes
24 modes
Backscatter Echo Width in dB>w!
25.00
15.00
5.00
-5.00
-15.00
-25.00
-35.00
0.00
30.00
60.00
90.00
120.00
150.00
180.00
Angle in Degrees

(b)

Fig. 7. Cont.

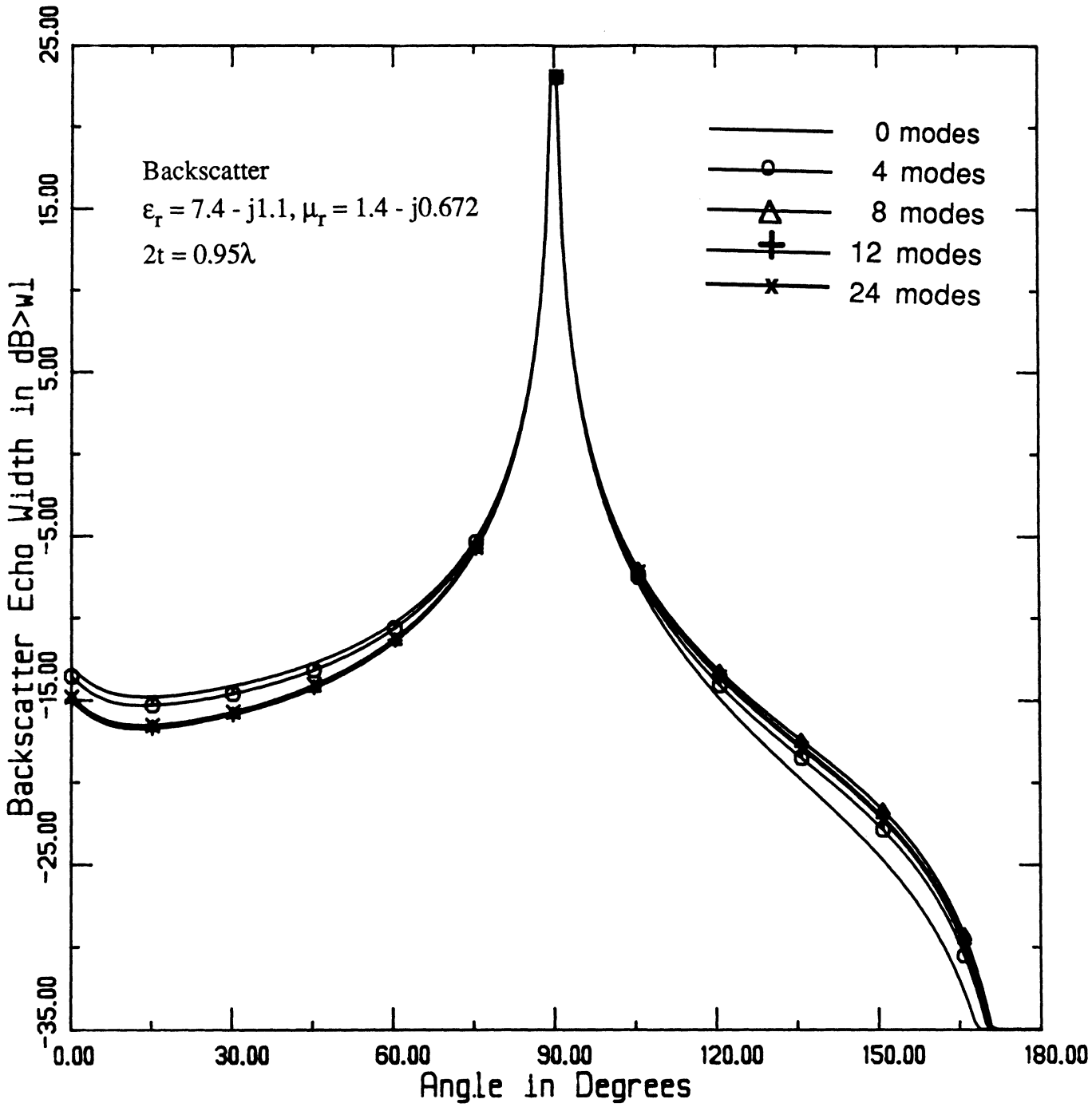
Backscatter
$\varepsilon_r = 7.4 - j1.1, \mu_r = 1.4 - j0.672$
$2t = 0.95\lambda$
0 modes
4 modes
8 modes
12 modes
24 modes
Backscatter Echo Width in dB>wl
25.00
15.00
5.00
-5.00
-15.00
-25.00
-35.00
0.00
30.00
60.00
90.00
120.00
150.00
180.00
Angle in Degrees

(c)

Fig. 7. Cont

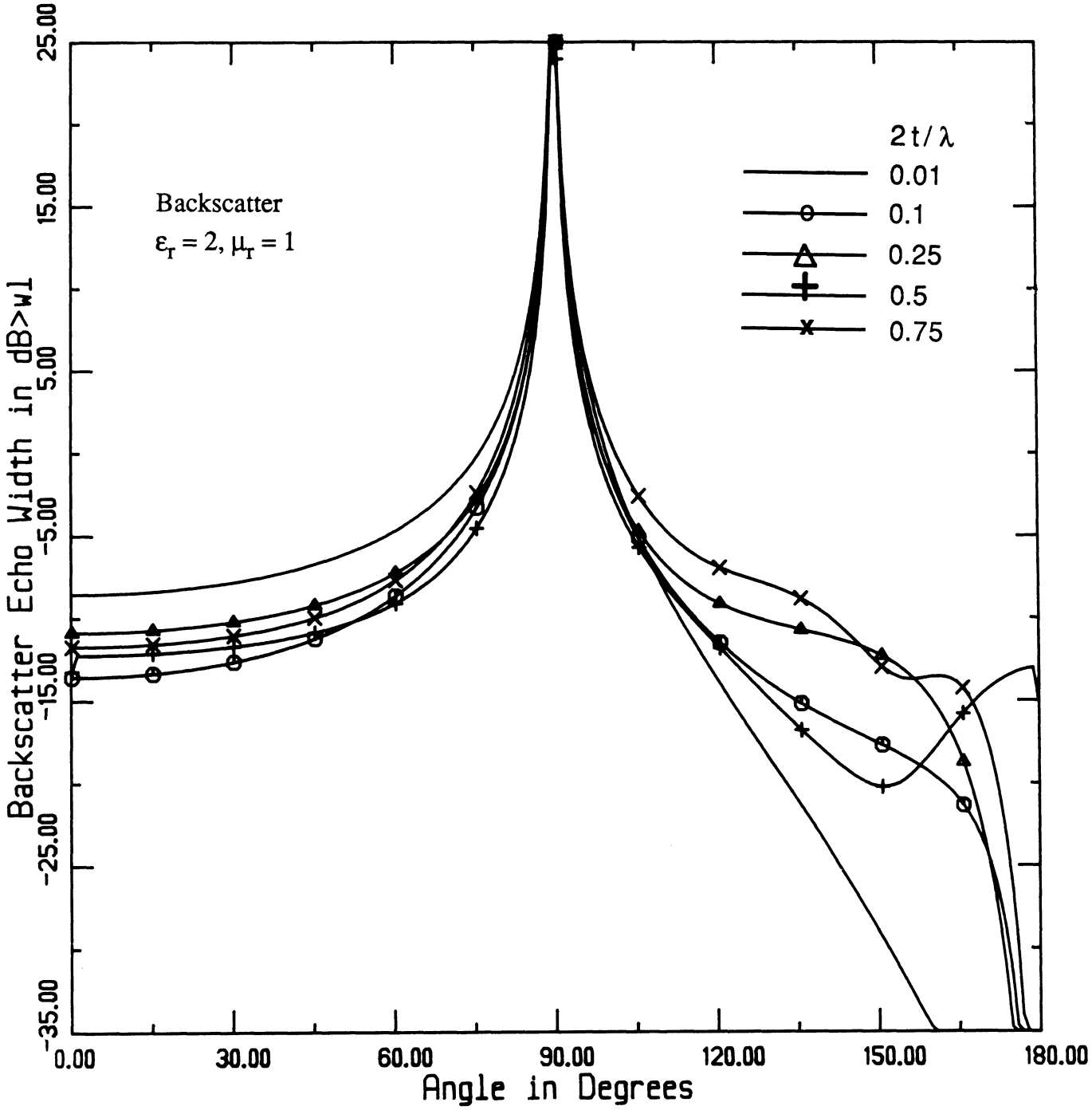

(a)

Fig. 8. H_z-polarization calculated echowidth family curves for 2t = 0.01, 0.1, 0.25, 0.5 and 0.75 wavelengths. The constitutive parameters of the dielectric are $\varepsilon_r = 2$, $\mu_r = 1$. (a) Backscatter case, (b) Bistatic with $\phi_o = 45°$, (c) Bistatic with $\phi_o = 150°$.

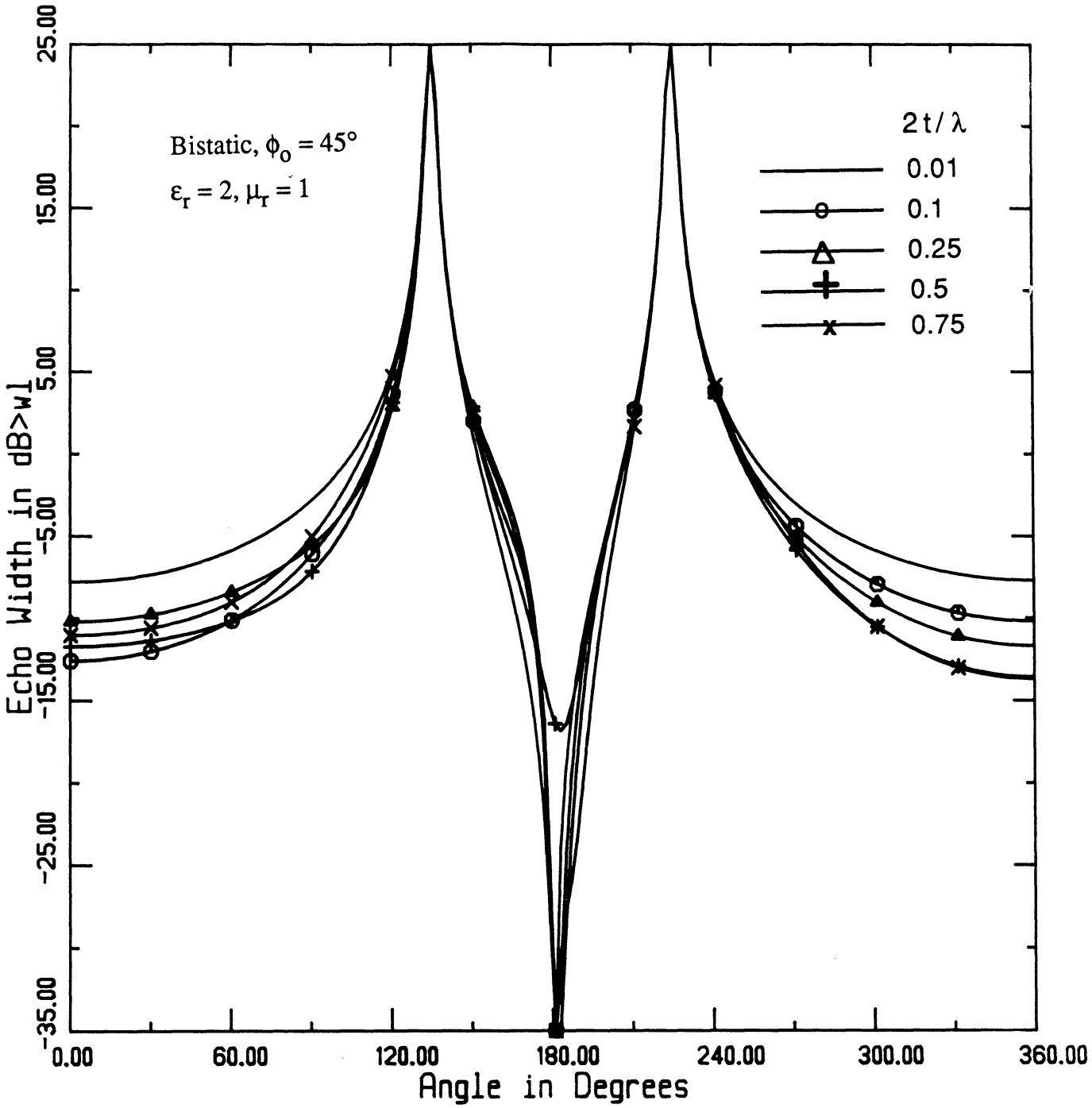
Bistatic, $\phi_o = 45°$
$\varepsilon_r = 2, \mu_r = 1$
2t/λ
0.01
0.1
0.25
0.5
0.75
Echo Width in dB>wl
25.00
15.00
5.00
-5.00
-15.00
-25.00
-35.00
0.00
60.00
120.00
180.00
240.00
300.00
360.00
Angle in Degrees

(b)

Fig. 8. Cont.

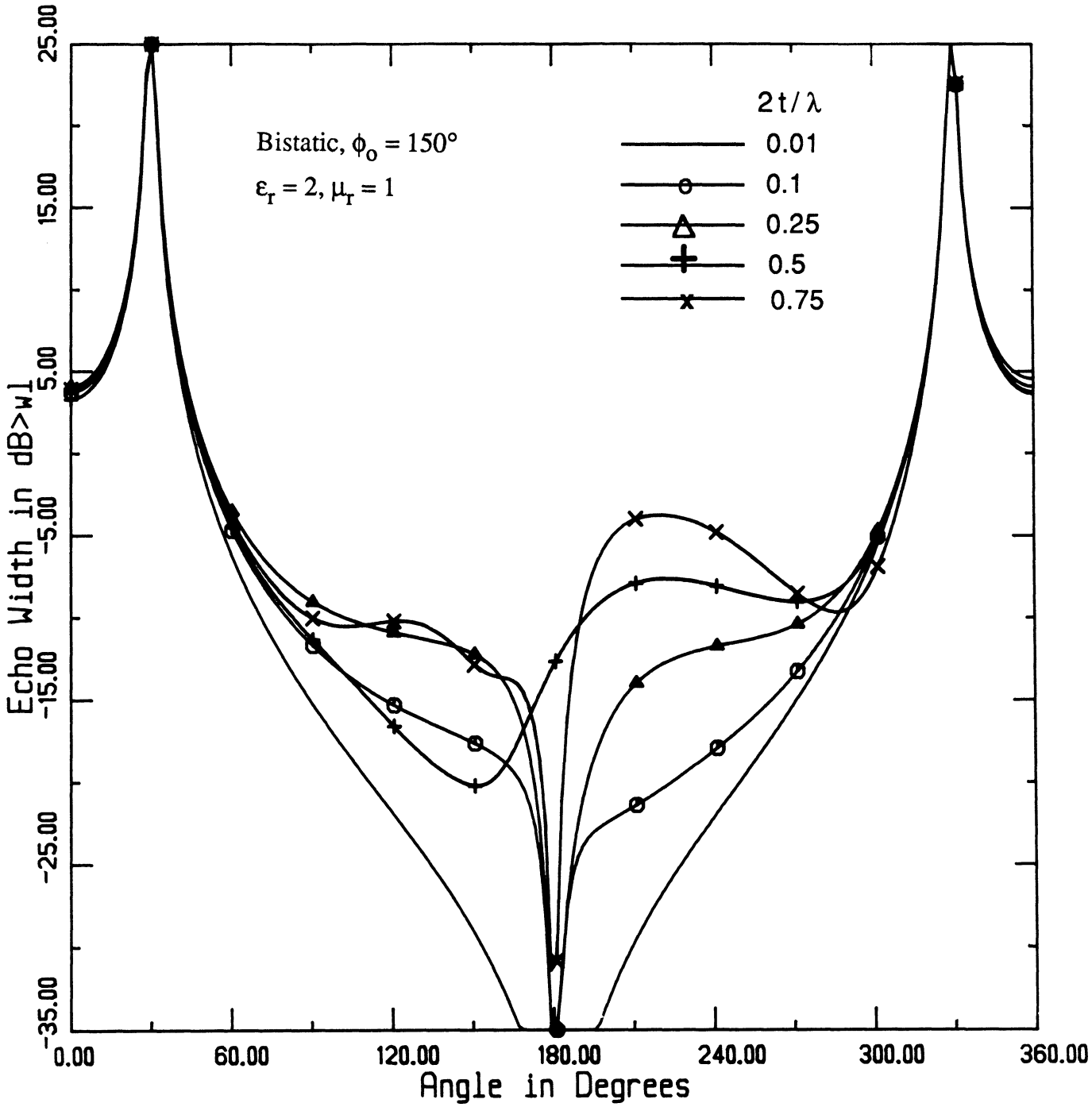
Bistatic, $\phi_o = 150°$
$\varepsilon_r = 2, \mu_r = 1$
2t/λ
0.01
0.1
0.25
0.5
0.75
Echo Width in dB>wl
25.00
15.00
5.00
-5.00
-15.00
-25.00
-35.00
0.00
60.00
120.00
180.00
240.00
300.00
360.00
Angle in Degrees

(c)

Fig. 8. Cont.

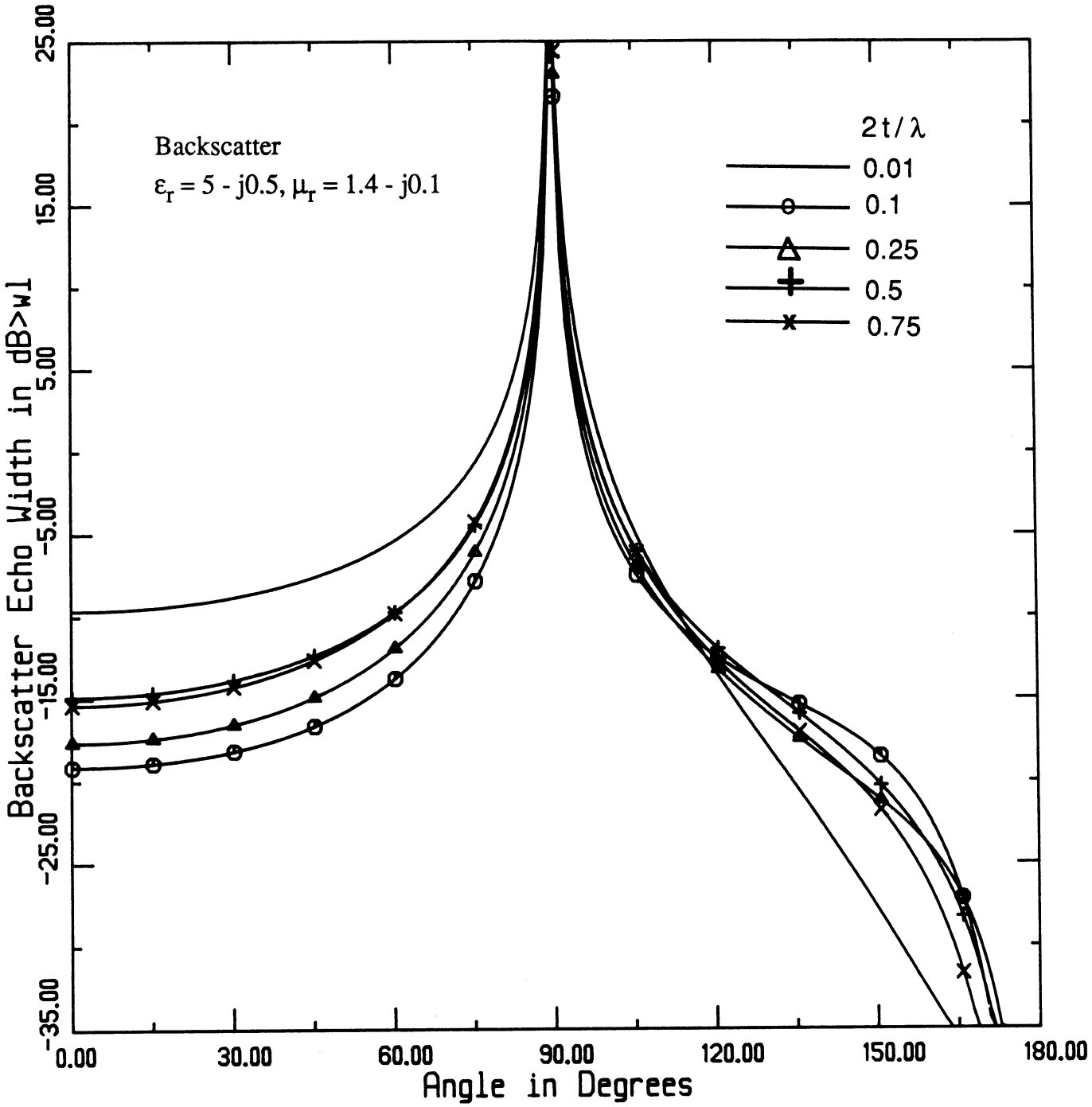

(a)

Fig. 9. H_z-polarization calculated echowidth family curves for 2t = 0.01, 0.1, 0.25, 0.5 and 0.75 wavelengths. The constitutive parameters of the dielectric are $\varepsilon_r = 5 - j0.5$, $\mu_r = 1.4 - j0.1$. (a) Backscatter case, (b) Bistatic, $\phi_0 = 45°$, (c) Bistatic, $\phi_0 = 150°$.

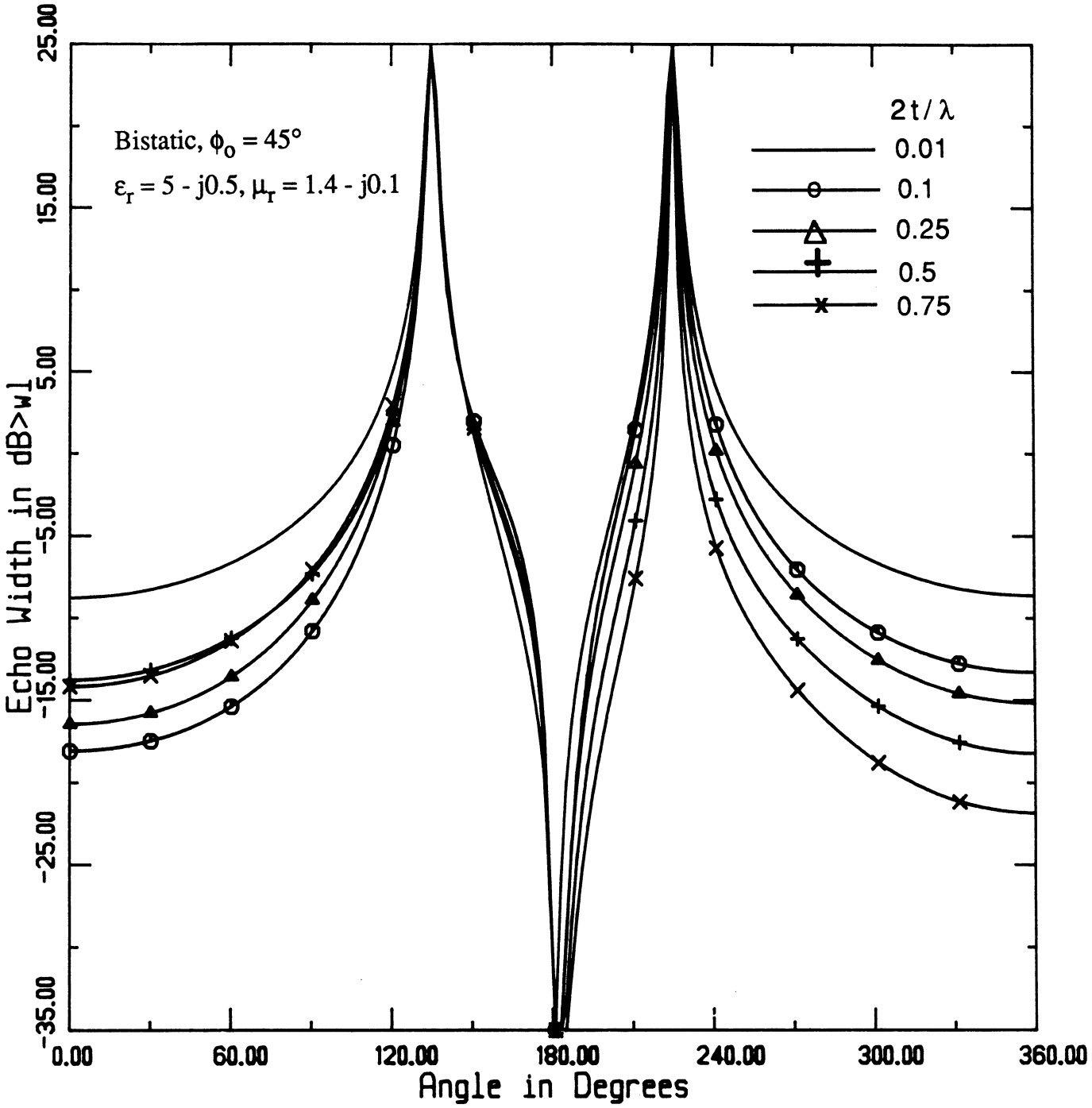
Bistatic, $\phi_o = 45°$
$\varepsilon_r = 5 - j0.5$, $\mu_r = 1.4 - j0.1$
$2t/\lambda$
0.01
0.1
0.25
0.5
0.75
Echo Width in dB>wl
25.00
15.00
5.00
-5.00
-15.00
-25.00
-35.00
0.00
60.00
120.00
180.00
240.00
300.00
360.00
Angle in Degrees

(b)

Fig. 9. Cont.

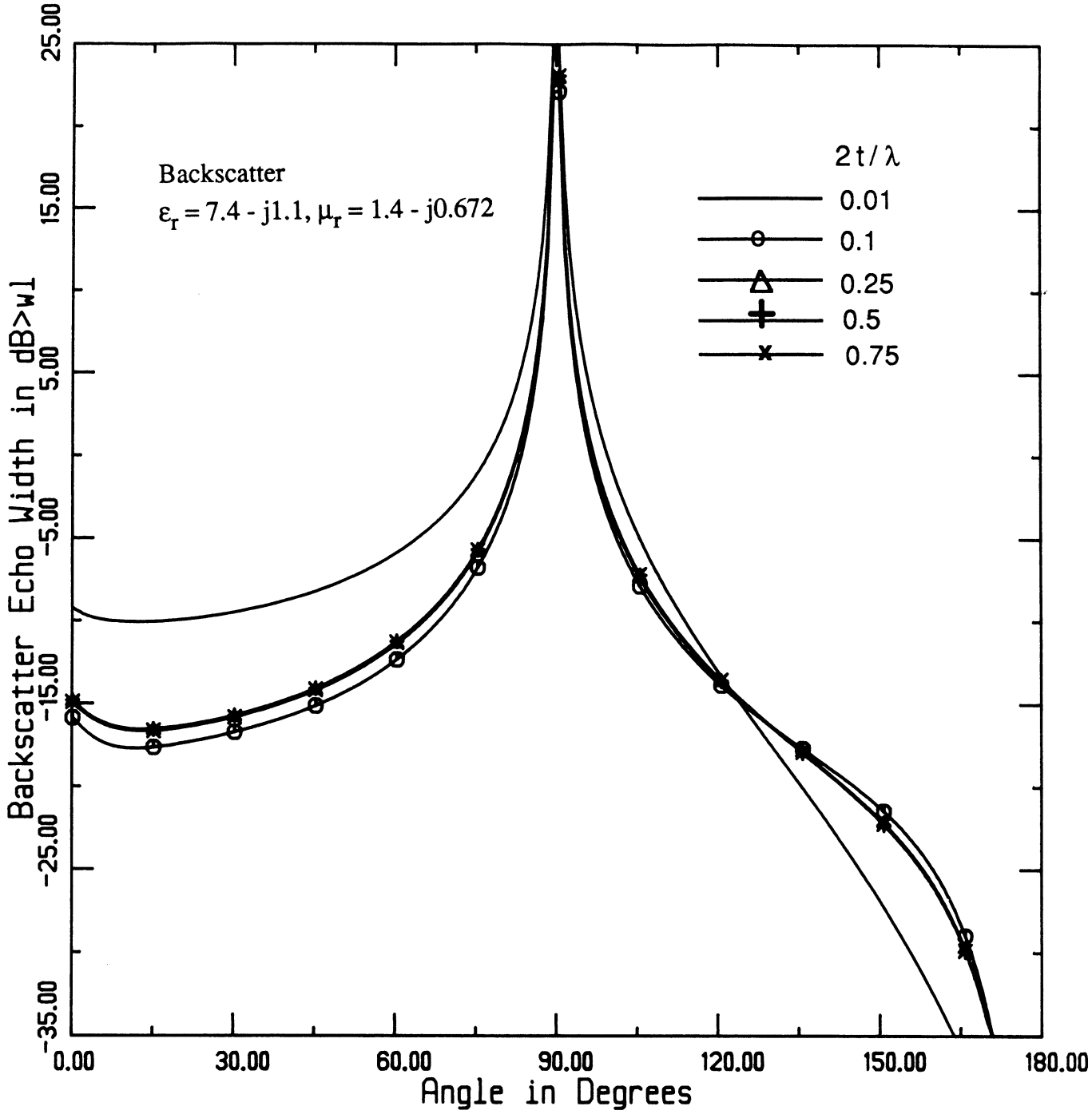

(a)

Fig. 10. H_z-polarization calculated echowidth family curves for 2t = 0.01, 0.1, 0.25, 0.5 and 0.75 wavelengths. The constitutive parameters of the dielectric are $\varepsilon_r = 7.4 - j1.1$ and $\mu_r = 1.4 - j0.672$. (a) Backscatter case, (b) Bistatic, $\phi_o = 45°$, (c) Bistatic, $\phi_o = 150°$.

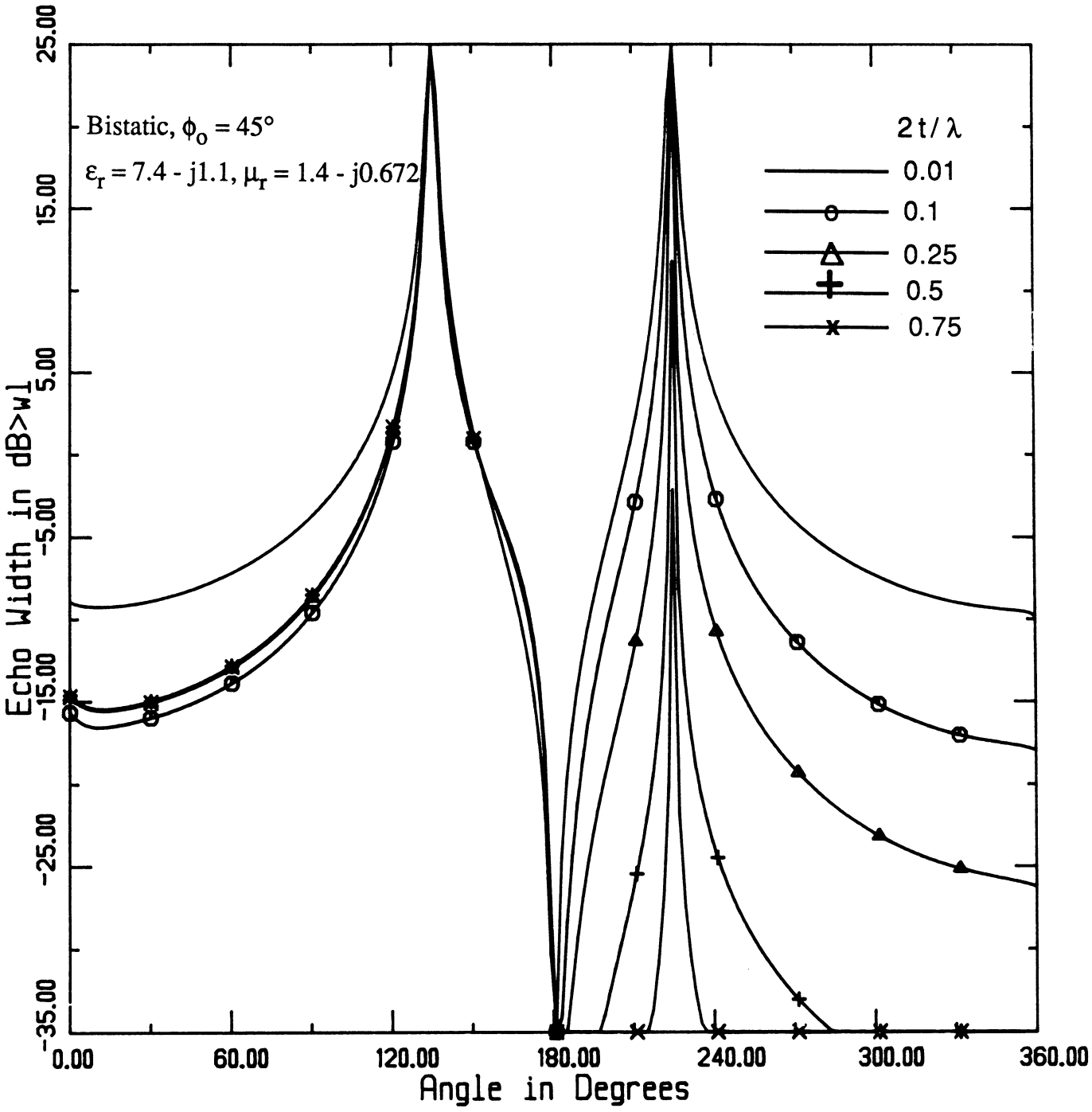
Bistatic, $\phi_o = 45°$
$\varepsilon_r = 7.4 - j1.1$, $\mu_r = 1.4 - j0.672$
2t/λ
0.01
0.1
0.25
0.5
0.75
Echo Width in dB>wl
25.00
15.00
5.00
-5.00
-15.00
-25.00
-35.00
0.00
60.00
120.00
180.00
240.00
300.00
360.00
Angle in Degrees

(b)

Fig. 10. Cont.

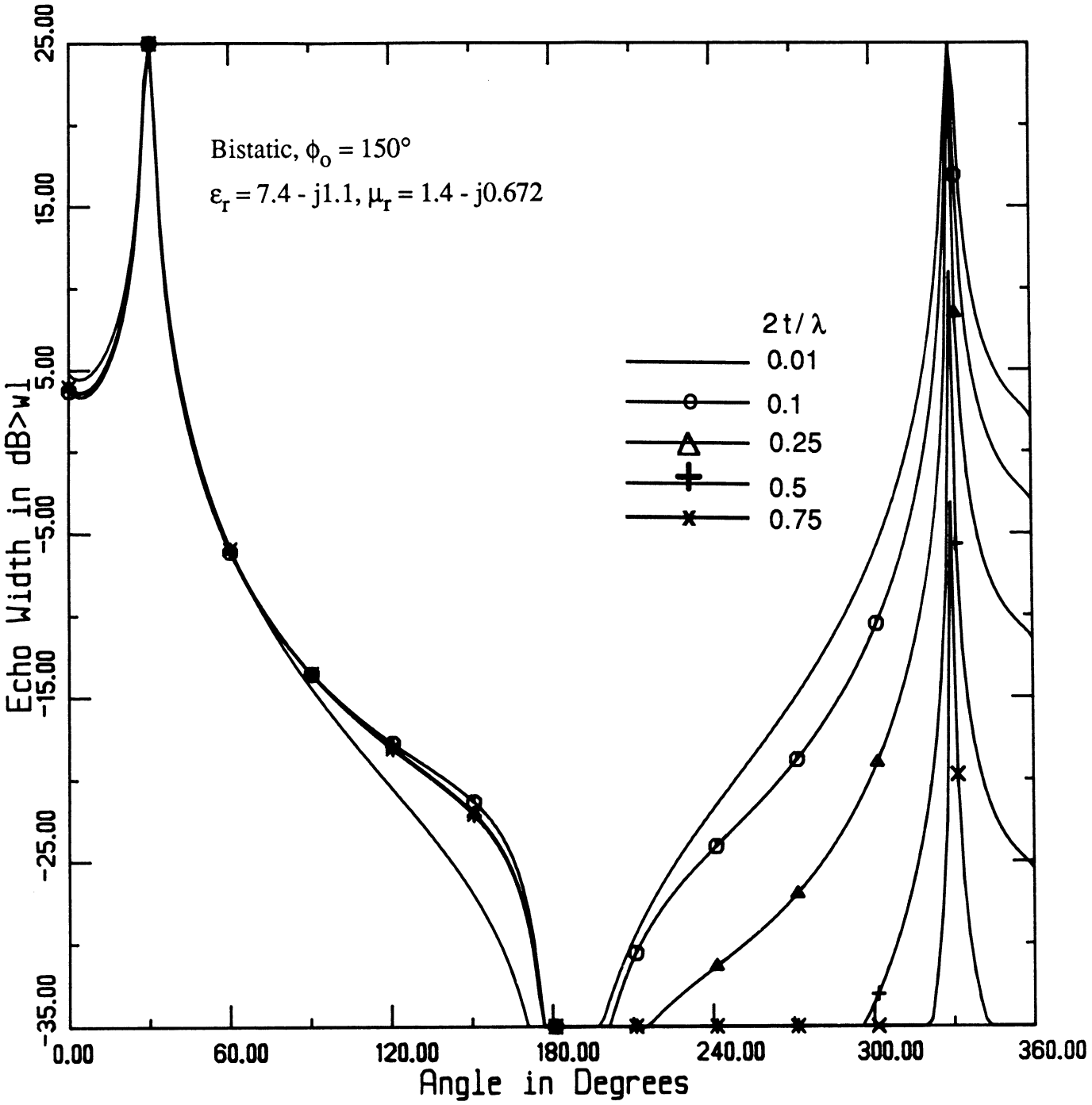
Bistatic, $\phi_o = 150°$
$\varepsilon_r = 7.4 - j1.1$, $\mu_r = 1.4 - j0.672$
$2t/\lambda$
0.01
0.1
0.25
0.5
0.75
Echo Width in dB>wl
25.00
15.00
5.00
-5.00
-15.00
-25.00
-35.00
0.00
60.00
120.00
180.00
240.00
300.00
360.00
Angle in Degrees

(c)

Fig. 10. Cont.

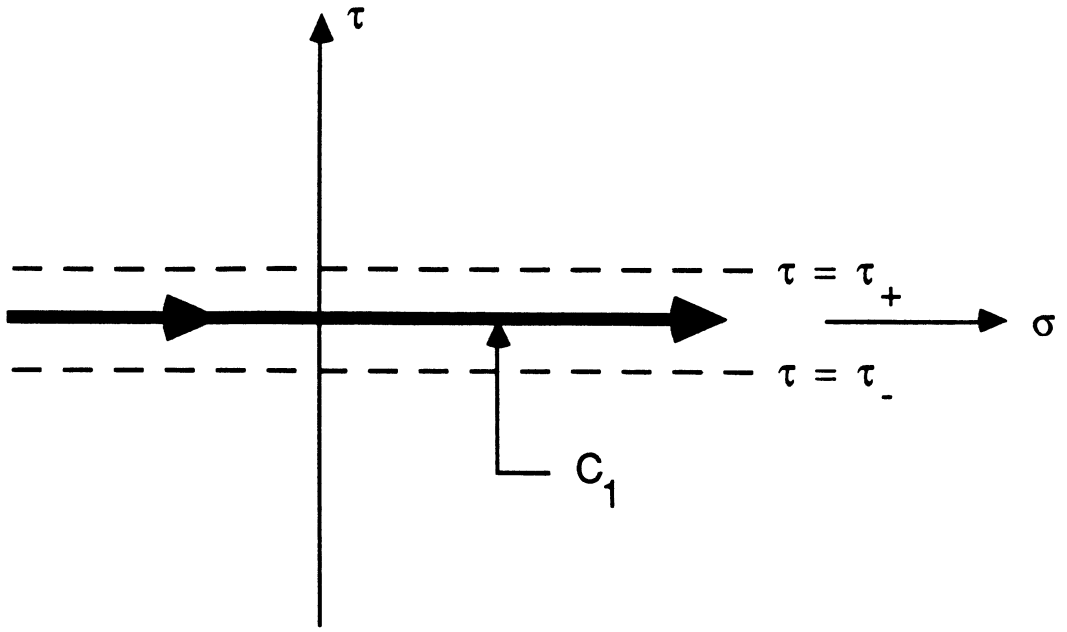

Figure B1. Illustration of C_1 contour.

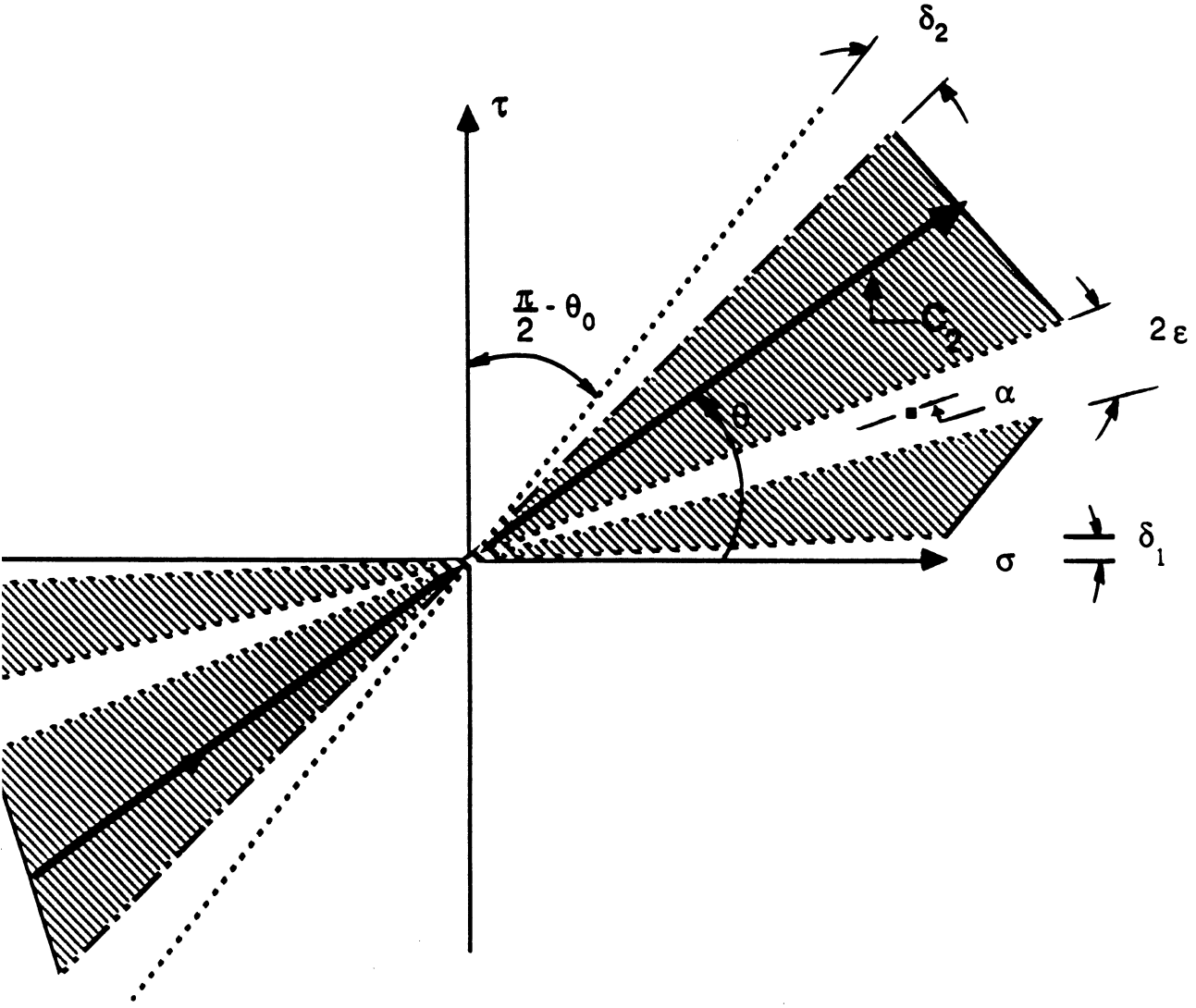

Figure B2. Illustration of the C_2 contour with the permitted values of θ.